Inelastic LIDAR for Monitoring Aquatic Fauna

LUND
UNIVERSITY

Master Thesis

Mikael Ljungholm

Thesis advisor: Dr. Mikkel Brydegaard

Division of Combustion Physics, Department of Physics at Lund University
Applied Molecular Spectroscopy and Remote Sensing (AMSRS)
Center for Animal Movment (Canmove)
Department of Biology at Lund University

March 2016

Mars 2016

Lund Reports on Combustion Physics, LRCP-194
ISNR LUTFD2/TFC-194-SE
ISSN 1102-8718

Mikael Ljungholm
Department of Combustion Physics
Department of Physics
Faculty of Engineering LTH
Lund University
P.O.Box 118
S-221 00 Lund
Sweden

Abstract

This thesis is oriented around designing the world first inelastic hyperspectral LiDAR(Light Detection and Ranging) system for aquatic use. The system was designed around the task of monitoring zooplankton and environmental indicators in water. Scheimpflug lidar was previously developed for monitoring flying insects, aerosols and gases. Here we extend the concept to inelastic hyperspectral ranging capabilities.

During the project, a novel system was developed that uses relatively low cost off-the-shelf components to create a compact LiDAR with both spectral, temporal and ranging capabilities making it a very versatile system with many possible applications such as, plankton and chlorophyll detection and assessment of water quality. The system uses a high power GaN laser-diode to emit a laser beam that propagates through the water. The laser light is then scattered both elastically (Mie and Rayleigh scattering), and inelastically (Raman scattering) by the water or by particles and plankton crossing the laser beam. The light might also be absorbed and result in fluorescence. The scattered light is collected by the receiving lens, after which the light is analyzed in term of energy for all distances along the line of view. The system was simulated using a raytracing program (FRED Optics by Photon Engineering) to find a feasible design with the available components. The system was assembled in a lab environment and calibrated. Lastly, the setup was tested in a 5-meter-long test-tank containing leaves and zooplankton of the genus Daphnia.

Acknowledgements

I would like to thank the following people for their contribution to this project.

To Mikkel who had the novel idea for the system. For allowing me to do this very interesting project. For all his help, advice and support throughout the entire project.

To Joakim for feedback and advice.

To Elin for encouragement, advice and help with the Schleimpflug principle.

To Samuel for his help in the lab.

To Guiseppe for help with constructing the experimental setup and suppling plankton for the test.

To Guangyu for his help in constructing the water-tank, help in conducting the experiments and analysis.

To Maria for help with images and support.

Contents

1. Introduction

1.1 Background

Plankton (phytoplankton and zooplankton) are small aquatic plants and animals ranging in size from the small bacterio-plankton at $0.2\mu m$ to megaplankton and long chains of plankton that can be over a meter long. The definition of what constitutes a zooplankton is not completely clear since many larger marine animals and plants also start their lifecycle in a plankton state [1]. In general when referring to zooplankton one refers to drifters. Figure 1.1 shows five examples of different types of zooplanktonon on a dark background. The figure shows an example of how size, shape and complexity can vary greatly. Most plankton have some sort of limbs (legs, fins, antennas, etc) that is used for propulsion.

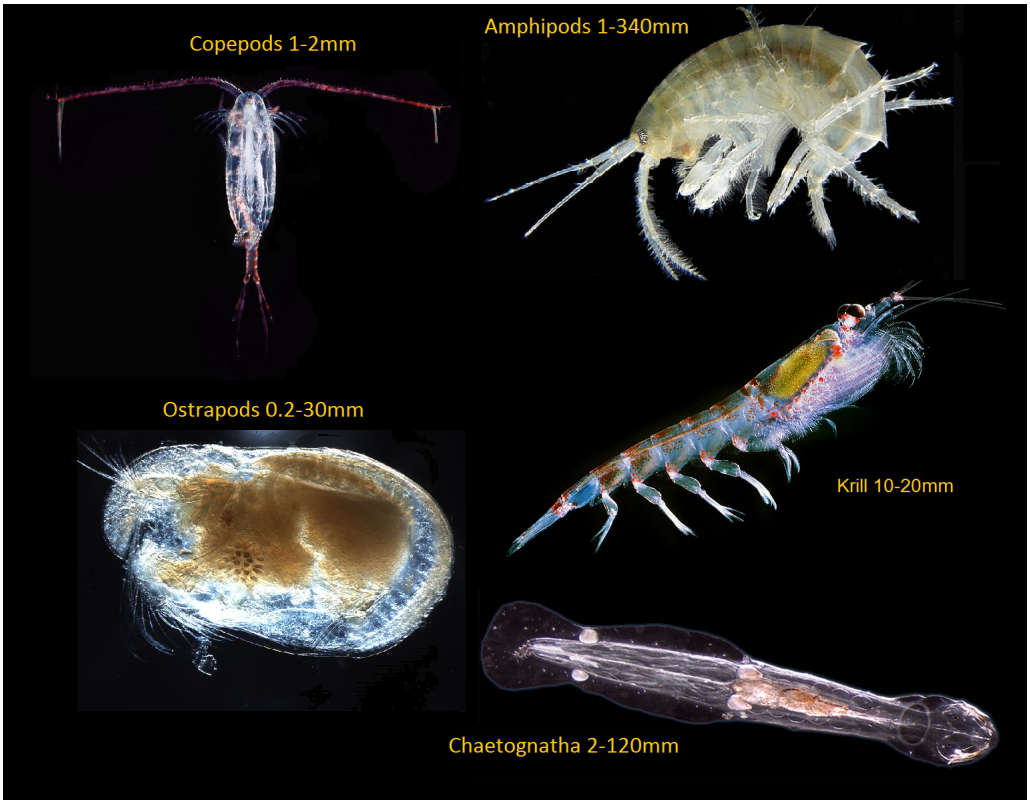

Figure 1.1: Zooplankton exist in many different species ranging from $0.2\mu m$ to meters in size. Many of the larger species have either legs or fins that they use to maneuver in their environment. (Images are adapted from Wikipedia)

The plankton used in this study is the *Daphnia magna*. The *Daphnia magna* is a common freshwater plankton that ranges in size from 1-5mm with the males usually not bigger than 2mm [2]. Figure 1.2 show a female *Daphnia magna* with the typical

morphological features of the genus Daphnia with a transparent carapace mostly composed of chitin.

Figure 1.2: Female *Daphnia magna* carrying eggs. Adapted from [2]

The ability to monitor plankton is of significant importance for several reasons. Plankton can be a great indicator of water quality sice the quality of water greatly affects the plankton populations. Compared to a water-sample that is very local in both time and space and can change in minutes or meters due to streams, plankton responds in days, accumulating effect over time. Suthers and Rissik states for instance that: "plankton are effectively our aquatic canaries -in-a-cage" [1]. Zooplankton that are of particular focus in this project can be indicator pH, oxygen and nutrients. They can also be used to monitor acidification, eutrophication (algae blooming), pesticide overuse and algal toxins [1, 3]. It is therefore of importance to study and monitor plankton. The conventional method of examining plankton population is by use of nets [1]. This method is both cumbersome and laborious, and even with automated suction devices the counting and identification is usually done manually. It is also often hard to define discrete depths and volumes with these methods. It is also challenging to only catch a certain type of plankton using nets since plankton of larger size also get caught in the net.

Zooplankton abundance often displays sharp layers in lakes and oceans. They also tend to migrate vertically in the water-column. This migration can be quite substantial moving almost the entire plankton population from the surface to depths between 10 to almost 100 meters [4]. Figure 1.3 is an image created by Ocean Networks Canada using the "Zooplankton Acoustic Profiler" [5]. It shows how population of plankton can move from surface to large depths in the timescale of a single hour making timing of importance in conventional sampling.

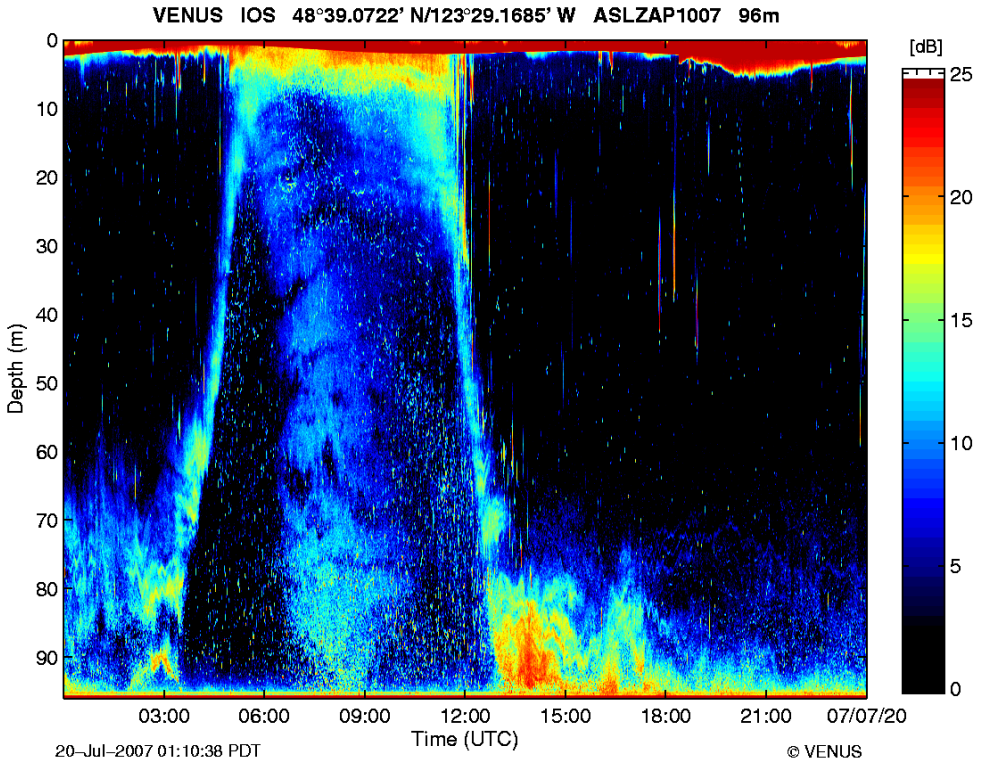

Figure 1.3: Example of vertical migration of zooplankton done with the Zooplankton Acoustic Profiler (ZAP). The colors represent the acoustic backscatter intensity. (Adapted from "Ocean Networks Canada" [5])

There are new emerging systems for plankton monitoring. The Video Plankton Recorder (VPR) for example [6], is an *in situ* systems that use cameras mounted on underwater robots utilizing shape recognition in order to count and identify the plankton. The zooplankton are small sparse particles, therefore it is challenging to focus on them. There is a new system that uses post focusing by digital in-line holography to solve that particular problem [7,8]. In our case, the focusing problem is solved with the Scheimpflug-hinge principle where angling of the lens and image-plane creates infinite focus.

Optical remote sensing can be a powerful tool in different types of monitoring situations. Among those systems, LiDAR (Light detection and ranging) is a system that have been proven to be useful and versatile. Conventional time-of-flight (TOF) LiDAR rely on photomultiplier tubes (PTM) and Si or InGaAs avalanche photodiodes (APD), both cooled. Recent development of CCD and CMOS technology has greatly reduced costs and improved performance, making CCDs and CMOS a viable option for LiDAR.

For aquatic purposes, there are a wide variety of remote sensing applications used presently. For example, satellite data are readily used to monitor environmental parameters in oceans and lakes such as chlorophyll and pollutions. There are LiDAR systems that can be used for the same purpose [9] and several LiDAR systems (mainly airborne). systems have been shown to be able to detect schools of fish [10–12]. There have been some studies on the use of airborne lidar to mon-

itor zooplankton [13, 14]. The NOAA (National Oceanographic and Atmospheric Administration) LiDAR system have been used to detect layers of plankton in the ocean and estimate the abundance of zooplankton. The NOAA LiDAR system uses a pulsed Nd:YAG laser with a photo-multiplier-tube detector setup to detect the elastic scattering of the zooplankton layers [15]. The NOAA LiDAR system could cover a large area quickly but it cannot detect individual plankton or distinguish between different plankton types. Since it only uses elastic backscattering it is the average biomass it detects. Further development of the system is required to ensure distinction between phyto-/zoo-plankton and schools of fish.

A LiDAR system can also be used to detect small individual objects like insects or plankton where radar would not work. The system proposed in this report will be based on previously constructed terrestrial LiDAR systems used for detection of flying insects [16, 17]. The system that was previously developed in our research group is capable of detecting individual insects and even resolve several harmonics of wing-beat frequencies. The cross-section scattering and wing-beat frequency of the insect may potentially be utilized for e.g. species identification [18]. Scattering LiDAR systems have also been used for monitoring of many other environmental properties like aerosols and gases [19].

To the writers knowledge there is currently no aquatic LiDAR system that can detect individual small elastic scattering particles and at the same time monitor inelastic signals.

1.2 Outline and aim of this thesis

The aim of this thesis was to create a system that can monitor the elastic scattering of zooplankton in a way similar to how the terrestrial system developed by Brydegaard et al. monitor atmospheric fauna constituents. The system should simultaneously be able to monitor inelastic Raman scattering from water and fluorescence from e.g. chlorophyll in aquatic fauna and flora.

The main part of the work was to create the hyperspectral lidar. This included creating and simulating a model of the system using ray-tracing and building and calibrating the physical device. Lastly, the system was tested in a lab-environment using a 5-meter-long water tank and live zooplankton.

The first part of this thesis will provide theoretical background on the principles of the different components. The second part describes the model creation, construction and experimental setup. The third part presents the collected signal detection. This is followed by a discussion and future outlook.

2. Theory

2.1 Range domain

Conventional LiDAR systems commonly use time-of-flight approach with pulsed lasers to ensure ranging capabilities. The LiDAR system proposed here is based on the Scheimpflug principle [20], using a continuous-wave (CW) laser. The range information can be calculated without the use of scanning mirrors and complex optics by using triangulation. System based on this principle have previously been used for atmospheric purposes [17, 19]. Figure 2.1 illustrates the Scheimpflug principle.

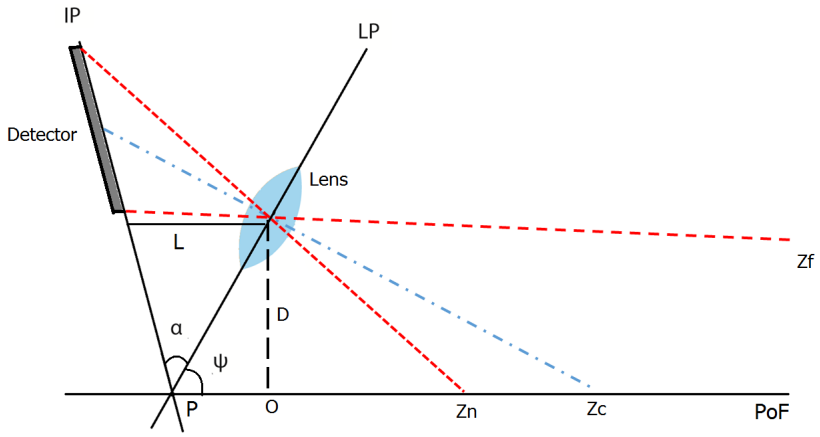

Figure 2.1: The Scheimpflug principle. The image-plane (IP), lens-plane (LP) and plane of focus (PoF) all intersects in one point "P" (Scheimpflug intersection). If the distance of the lower edge of the detector and the lens (L) is one focal length, then all points along the PoF will be focused on the detector, e.g. infinite focal depth is achieved. Zn, Zc and Zf are the distances from origo to the closest detectable distance, the distance correlating to the center of the detector and the furthest detectable distance respectively.

In a conventional imaging system the lens-plane (LP), the image/detector-plane (IP) and the plane of focus (PoF) are all parallel. To focus on different distances the distance between detector and lens or focal length has to be changed. If the lens or detector is tilted, it will cause the detector plane and lens plane to intersect at the point "P". The intersection of the LP and IP will also tilt the plane of focus thus making it possible for points of different distance to be focused at the same time. A simple use of this is if the distance of the lower part of the detector and the lens (L) is one focal length. Then all points along the PoF will be focused on the detector. This creates an infinite focal depth while still employing a large optical aperture essential for collecting light needed for spectroscopic use. The distance to a scattering point for a signal on the detector can then be calculated by simple

geometry and optical laws or calibrated with known distances.

In the case of aquatic use, imaging infinite distance is not preferred since the signal will be limited by water attenuation, resulting in a portion of the detector being unused. Instead a near field approach that also allows for a closer near field point is preferred. In this case the Schleimpflug rule alone does not guarantee that the points along the PoF are in focus on the detector, only that they have the possibility to be. To ensure focus of all points along the PoF the Scheimpflug principle must be complimented by the hinge rule [20]. The front focal plane (FP) of the lens and the plane parallel to the detector through the center of the lens must also intersect at a line on the PoF. See figure 2.2

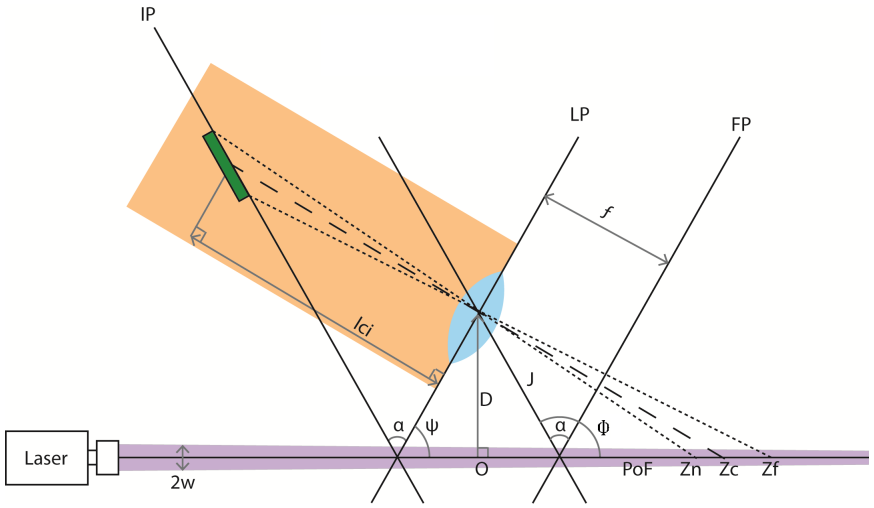

Figure 2.2: Scheimpflug-hinge rule. The lens-plane (LP) and image-plane (IP) intersect the plane-of-focus (PoF) at the same point. The focal-plane (FP) and the plane parallel to the image-plane (IP) that goes through the center of the lens must also intersect PoF to ensure focus in all points along the laser-beam. f is the focal length of the lens. D is the distance between center of the lens and the laser beam. lci is the distance from the center of the detector to the lens. The probe volume is dependent on the beam diameter given by the Gaussian beam parameter 2w and the part of the beam that is imaged on the detector

The distance parameters Zn, Zc and Zf are dependent on the variables f, lci, D, α, Ψ and size of the detecor, which in turn are not independent variables. If the size of the detector, f and angle α are set then Zn, Zc and Zf are reduced to a function of the distance lci which in turn determines the tilt angle Ψ and distance D.

2.2 Spectral domain

2.2.1 Inelastic signals

There are two main processes for inelastic signals of interest for our purpose, fluorescence and Raman scattering. The common type of fluorescence occurs when a

substance emits light at a longer wavelength than the absorbed light. The absorbed light excites the molecules to a higher energy state. The energy state is then for larger molecules often lowered by a non-radiative relaxation process. Finally the substance returns to a lower energy state by spontaneous photon emission with a lower photon energy than the absorbed energy [21]. Figure 2.3 is an example of a molecular fluorescence process. Light is absorbed from the ground electronic level to an exited electronic level. The energy is then reduced to a lower vibrational energy-state by relaxation. The molecule then returns to the ground electronic state via photon emission. The transition to the ground state can occur to one of several vibrational levels in the ground electronic state often resulting in a broad fluorescence spectrum.

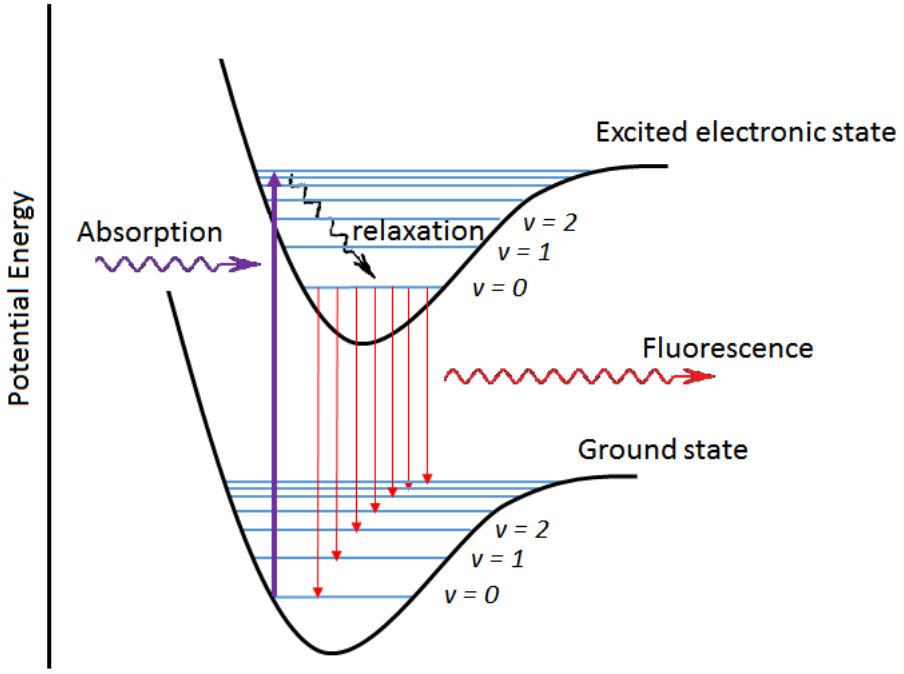

Figure 2.3: Jablonski diagram of molecular energy-levels displaying a fluorescence process for a larger molecule (smaller molecules does not always lose energy by relaxation).

Chlorophyll is a pigment molecule of interest since it is present in phytoplankton which are an important part of the zooplankton foodchain. Figure 2.4 show the absorption and fluorescence spectrum of Chlorophyll *a*, the most common chlorophyll type in phytoplankton [22, 23]. Chlorophyll b is mostly found in phytoplankton at deeper water levels [24]. The absorption and fluorescence peaks are partially overlapped so that the first emission feature can be reabsorbed by the same Chlorophyll. Chlorophyll b have a first absorption peak shifted to the red at around 460 nm and the second absorption and fluorescence peak at around 650 nm.

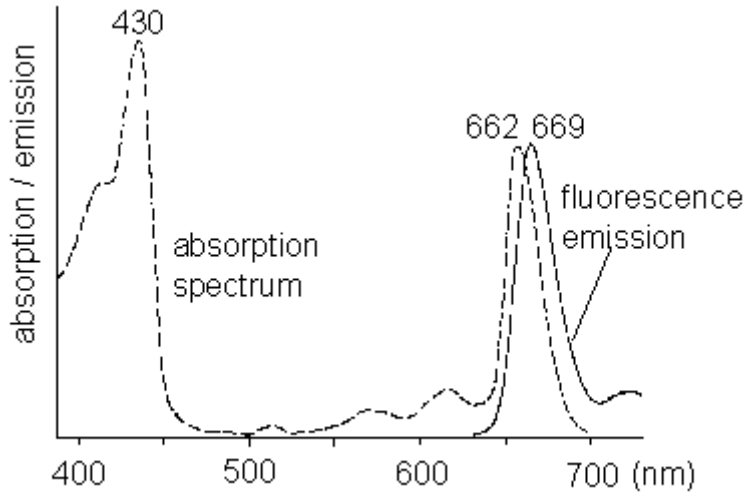

Figure 2.4: Absorption and fluorescence spectrum for chlorophyll a (Adapted from [25])

Raman scattering is an inelastic scattering process related to the elastic Rayleigh scattering. Light incident on a polarizable molecule can instantly excite and decay from a virtual energy level to a different vibrational energy level than before and scattering the light with an energy change corresponding to the vibrational energies [21]. If the scattered light loses energy which is the most common process, it is called Stokes-shift. The more uncommon process where the light gains energy is called anti-Stokes-shift. Figure 2.5 illustrates the Raman processes and the relation to Rayleigh scattering. Like the Rayleigh scattering, the Raman scattering likelihood scales with λ^-4 The wavelength of the Raman signal is thus dependent on the excitation wavelength. The Raman shift for water is dominated by the H-O stretch around 3400 cm^{-1} [26–28]. For an excitation wavelength of 445 nm this would put the vibrational water-Raman peak at about 524 nm (The shift expressed in wavelength increases with excitation wavelength).

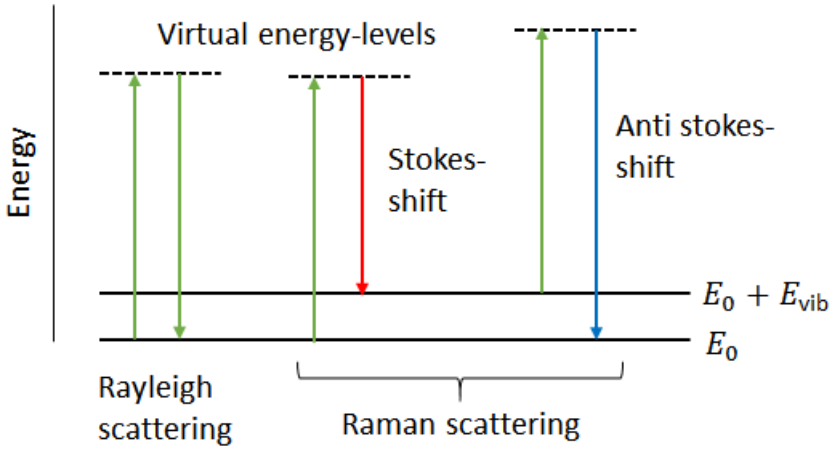

Figure 2.5: Jablonski diagram showing Rayleigh and Raman scattering. E_0 represents the ground energy state and E_{vib} is the excited vibrational energy-level

2.2.2 Wavelength separation

To separate the wavelengths of the collected light a Pris-Grating-prism configuration (PGP) [29] was chosen. The PGP described below has the advantage of separating the spectral spectral band in one dimension while at the same time retaining the spatial information gained with the Scheimpflug construction.

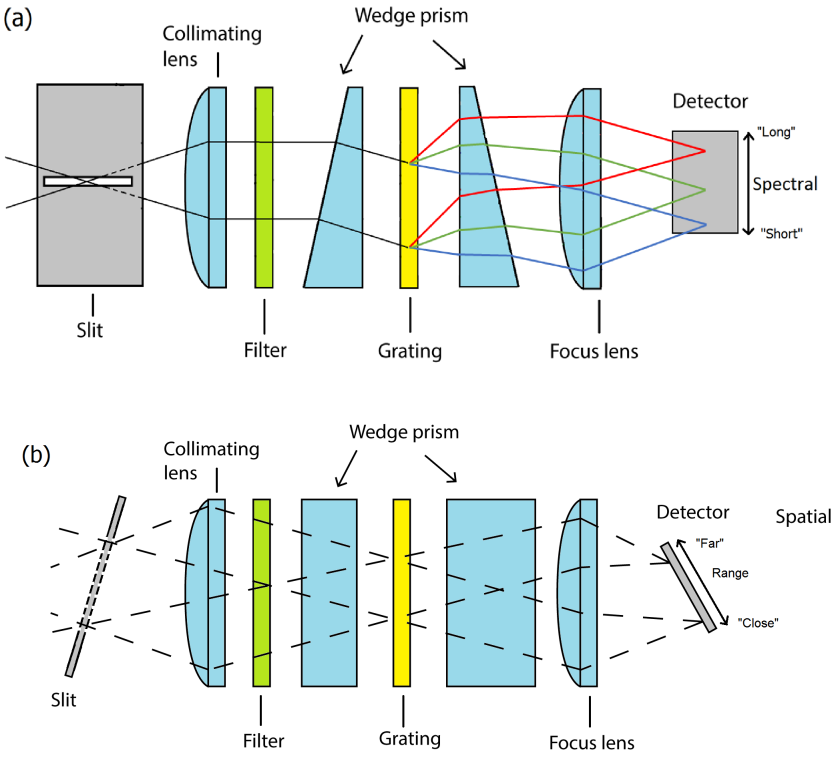

Figure 2.6: (a) "spectral view" of the PGP. The light enters from the slit as a narrow point-like source that is collimated by the first lens. The light passes through the two prisms and the grating to disperse the frequencies and direct the light which is then focused on to the detector.(b) "ranging view" of the PGP The spatial information is retained when passing though the PGP.

The PGP was invented by Mauri Aikio and its principle construction is composed of five parts (figure 2.6) [29]. Two lenses, two wedge prisms and one transmission grating as the spectral dispersive component. This does not include the light collecting optical components, the detector or any filters. The main advantages of the PGP is that it can be made of relatively cheap components and that the optical axis of the light remains relatively unchanged.

The purpose of the first lens is to collimate the light from the entrance slit. The first wedge-prism then refracts the light "down". The light is then dispersed by the transmission grating. The grating is oriented so that the strongest diffraction order is directed "up". Since the light was incident at an angle the 0^{th} diffraction order will

continue "down" and thus be diverted from the detector. The second wedge-prism then once again refracts the the light "down" to compensate for the angling of the grating. The last lens focuses the light on to the detector. A simulation of the PGP can be seen in figure 3.3.

The grating used is a blazed transmission grating. The transmission power is thus dependent on wavelength, grooves/mm and grove-angle. Maximum power for the 1^{st} order is achieved by matching the refraction angle though the wedges (see fig 2.7) that make up the grating to the diffraction angle given by the grating equation [30].

Peak efficiency for 1^{st} order for a wavelength λ is given by

$$\lambda = (n-1)dsin(\chi) \tag{2.1}$$

Where n is the refractive index of the grating, χ is the blaze angle and d is the groove spacing.

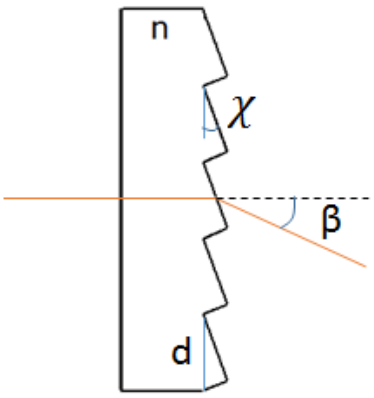

Figure 2.7: Blazed transmission grating. The angle χ is the blaze angle, d is the groove spacing and n is the refractive index for the grating.

Figure 2.8 shows some typical transmission curves for blazed transmission gratings. As can be seen in the figure, the 1^{st} order diffraction can be as strong as 70%. Thus if the grating is oriented properly in the PGP the 1^{st} order will be stronger than the 0^{th} diffraction order.

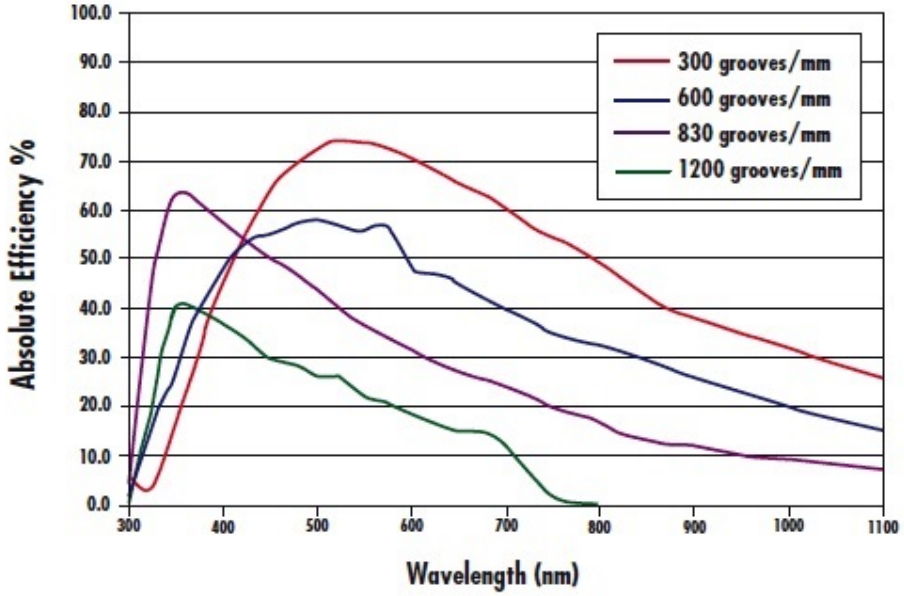

Figure 2.8: The plot shows transmission efficiency for the 1^{st} order for different groove spacings. In this case the blaze angle for the red curve is 17.5° [31]

2.3 Temporal domain

In order to resolve the oscillations in the elastic cross section of the zooplankton caused by the movement of the plankton legs etc, the signal capture system needs to be fast enough. The minimum sampling frequency needed is determined by the Nyquist frequency:

$$f_N = f_s/2 \tag{2.2}$$

Where f_S is the sampling frequency. Since the oscillations of the zooplankton vary between different spices the sampling frequency will also vary. The most limiting factors for sampling frequency is the fps (frames/second) of the camera and the data transfer rate to the computer or other storage unit. One example of an oscillating zooplankton is the *T.longicornis*, that oscillates at around 40Hz [32]

3. Methods

3.1 Ray tracing

Ray tracing is a way to simulate optical systems where the light is represented by rays that propagates though the system. The rays are subjected to refraction at the different surfaces to determine the path. By tracing many individual rays the response of the full system can be simulated. This is a very useful tool when the components of a system cannot be easily described with simple equations. One great advantage of this approach is the ease at which aberrations and stray light can be spotted.

Ray tracing of the system was done in several parts. The equations for the near field Scheimpflug-hinge-principle was tested. The PGP was simulated in several steps to see if it would work together with the Scheimpflug-hinge setup. The system was finally simulated many times with different optical components in order to find a set of off-the-shelf optical components that would fulfill the need of the setup.

The program used for the ray-tracing was Fred Optical Engineering Software (FRED) created by Photon-Engineering. It is a commercial 3D-CAD optical engineering program.The figures 3.1-3.3 show the simulation of the optics.

The ray tracing was done in several steps in order to test the function for each part before simulating the complete construction. Figure 3.1 shows a reduced example of the final model. The full model used approximately 11000 rays to simulate the incident light. The final version also used Zemax models for the lenses provided by the reseller.

Figure 3.4 is an example of a ray trace done to ensure that only the first order diffraction from the grating hit the detector. As can be seen in figure 3.4 proper precautions has to be taken regarding the shielding around the spectrometer to avoid unwanted stray light reflections.

Figure 3.5 and 3.6 are examples of simulations testing the focus on the detector when the Scheimpflug-hinge condition is fulfilled. Figure 3.5 is a surface intersection test on the detector with 5 point sources at 5 different distances, all with 5 different wavelengths each. Figure 3.6 is a 3D intensity plot of light hitting the detector to simulate the FWHM spot size of different point sources.

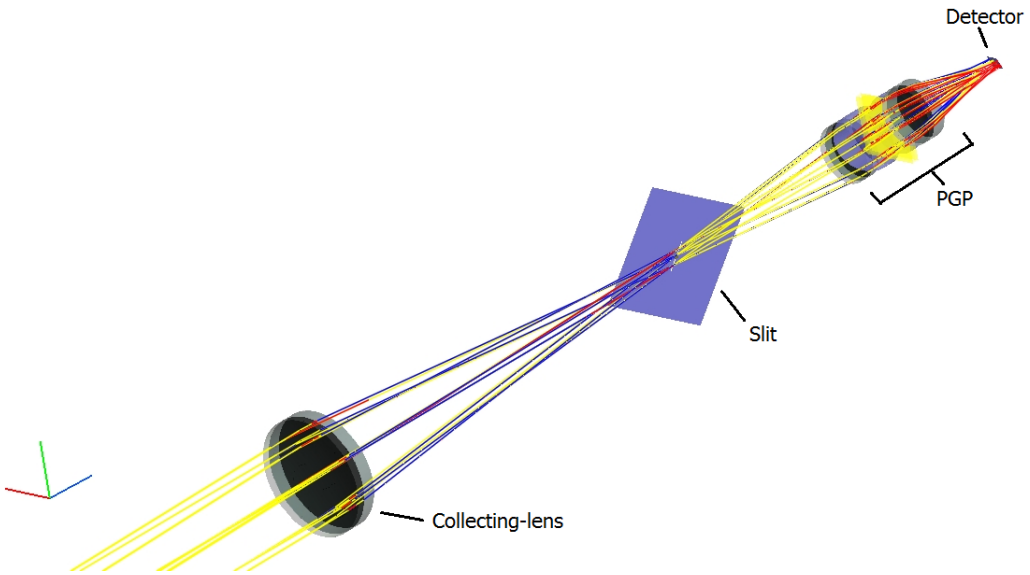

Figure 3.1: A screen capture of the simulation. In the image the PGP can be seen together with Scheimpflug-hinge configuration. Rays from several distant point-sources with three different wavelengths are shown.

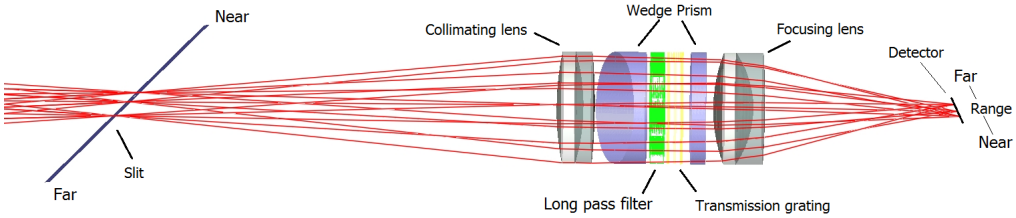

Figure 3.2: Top view of the slit, PGP and detector. Three point-sources at different distances are all focused onto the slit with the Scheimpflug-hinge rule. The range information is preserved though the PGP.

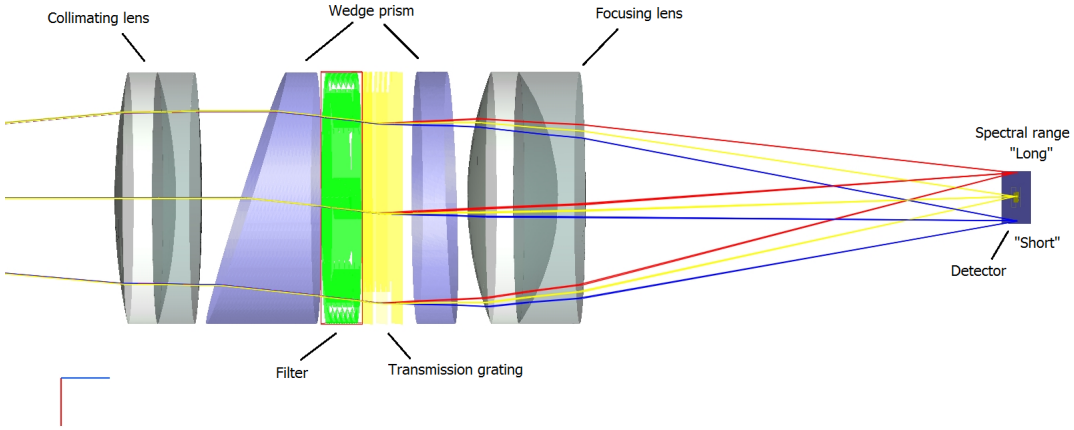

Figure 3.3: Side view of the PGP and detector. Light from one point-source is diffracted by the grating and focused on the detector.

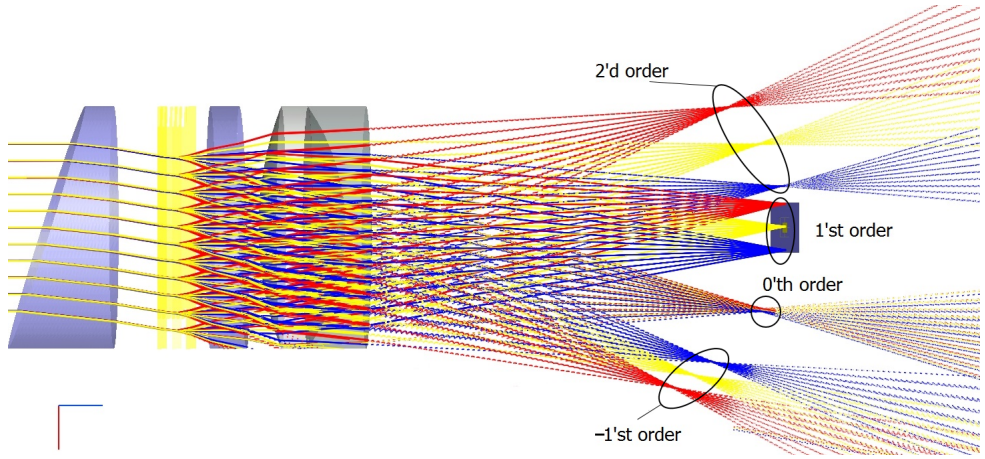

Figure 3.4: Ray-tracing simulation using multiple diffraction orders. The simulation was done to ensure that only the 1^{st} order diffraction hit the detector.

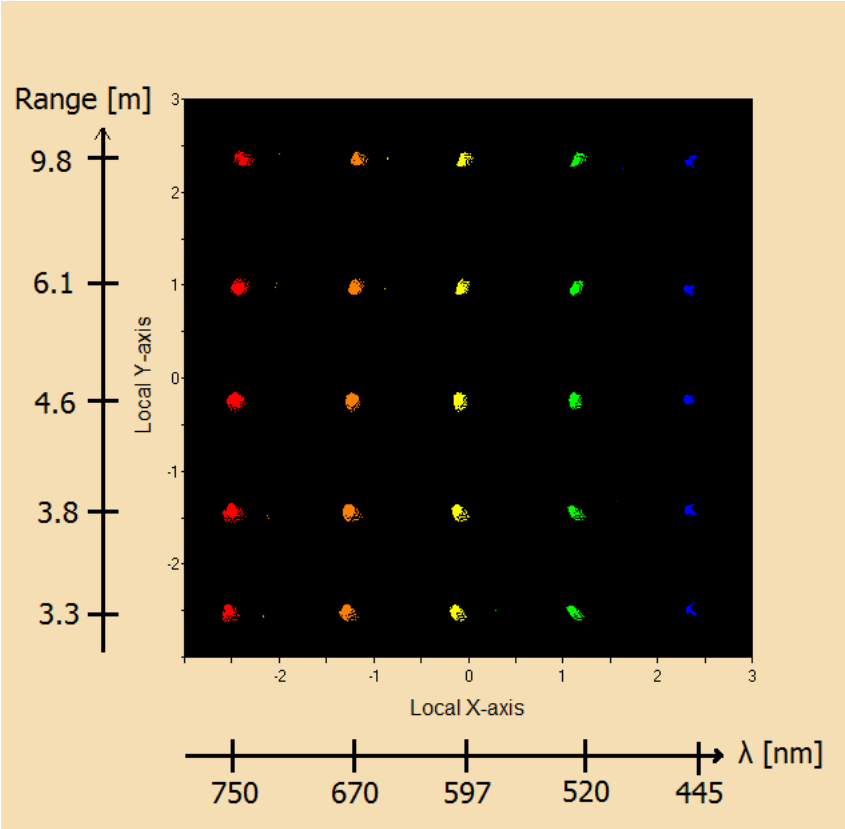

Figure 3.5: Spot diagram resulting from the simulated detector using several multi-wavelength point sources along the theoretical line of focus.

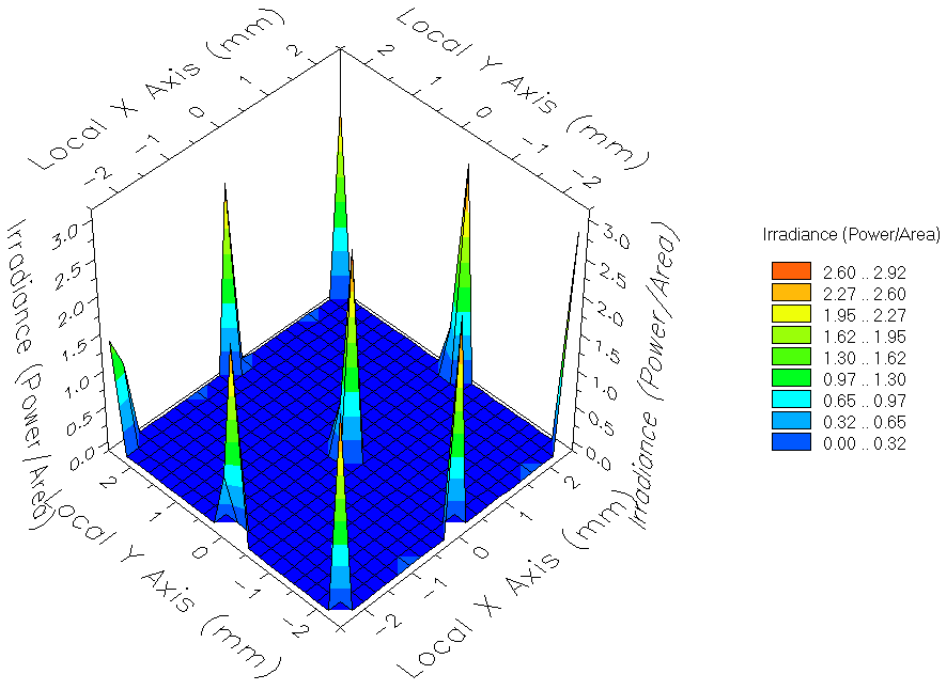

Figure 3.6: Intensity function of the spots on the detector resulting from the retracing of the setup.

3.2 Components and construction

3.2.1 Optics

The lenses used are all AR coated achromatic doublets. The objective lens is 50mm diameter with 200mm focal length.

The lenses in the PGP are both 25mm diameter with 100mm and 50mm focal length respectively.

The grating is a 25mm square 300grooves/mm blazed transmission grating with a blaze angle of 17.5^o. This was later cut to a circle to fit with the other optics.

The wedge prisms are both 25mm diameter prisms with an angle of 11.21 and 7.41 respectively.

The long pass filter is a 25mm diameter OD2 Longpass filter with a cut-off below 450nm.

The slit is handmade and constructed by fixing two razorblades to a brass frame. The spacing was created by stringing $200\mu m$ copper wires between the blades and removed after the blades where fixated.

The lenses, prisms, gratings and filter was bought from Edmund Optics. The efficiency for the grating and the longpass filter can be seen in figure(3.7) below.

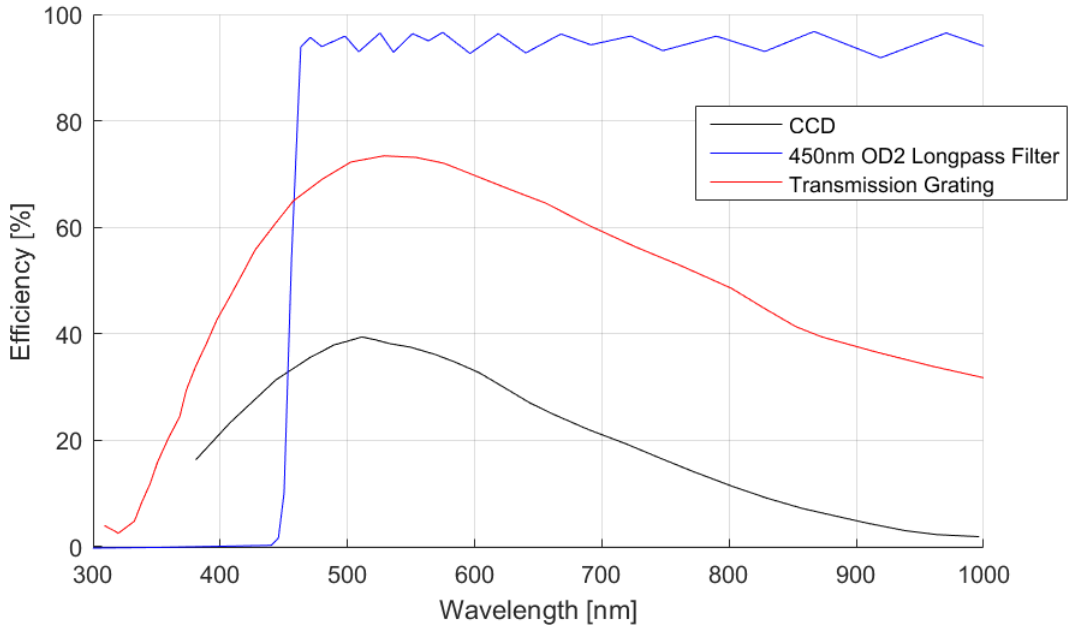

Figure 3.7: Composite curve showing the transmission efficiency for the grating and the longpass filter together with the quantum efficiency for the CCD.

3.2.2 Emitter

The emitter uses a 1W GaN laser diode at 445nm from a chip source size of 1x20 μm. The laser light is expanded, collimated and transmitted by a standard video objective with $\varnothing = 20mm$ and $f_{exp} = 20mm$. The objective has an adjustable focus and iris for beam shaping.

3.2.3 Detector

The detector is a CCD detecor on a ATV Prosilica GC655 camera. The detector has 659x493 pixels with a total size of 6,5x4.9mm. The signals detected by the pixels that make up the detector can be bound together, effectively making larger pixels resulting in faster operation of the detector (higher frame rate) at the cost of lower resolution. This process is called binning. Figure 3.8 shows the binning specification by the manufacturer.

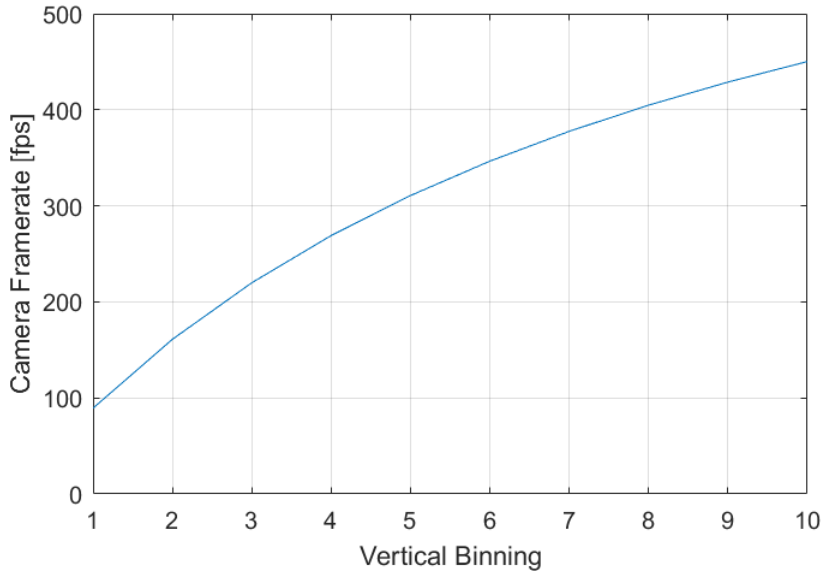

Figure 3.8: Camera frame rate specified by the manufacturer. The frame rate can only be increased by binning the vertical pixels which translates into the spectral domain in the setup.

3.2.4 Mechanics

The mountings for the lenses and prisms are standard mountings for 1- and 2-inch optics from Edmund Optics and Thorlab. The 50 mm objective lens is mounted with an adjustable mount to enable focusing.

The laser is mounted on two rotation mounts from Edmund Optics to enable elevation and azimuthal alignment. This in turn is mounted on a slider on a Dovtail-rail to enable lateral shift of the laser.

3.2.5 Electronics

A current generator was used to power the diode laser. A laptop connected by a Gig-E cable to the camera was used to capture and store the images.

3.3 Experimental setup

The setup was assembled on an optical bench and aligned by some simple methods described below.

The first part to be assembled and aligned was the PGP. Figure 3.9 below illustrates the procedure. A small class II red laser was aimed through the mountings for the PGP optics and blocked with a screen. The first prism was then inserted and rotated so the spot on the screen moved straight down along the vertical axis. The grating was then inserted and rotated so that the -1st and 0th order was both on the vertical line. Finally the second prism was inserted and rotated so that the -1st order was moved down but still on the vertical line. The components where then fixed and mounded on the rest of the setup.

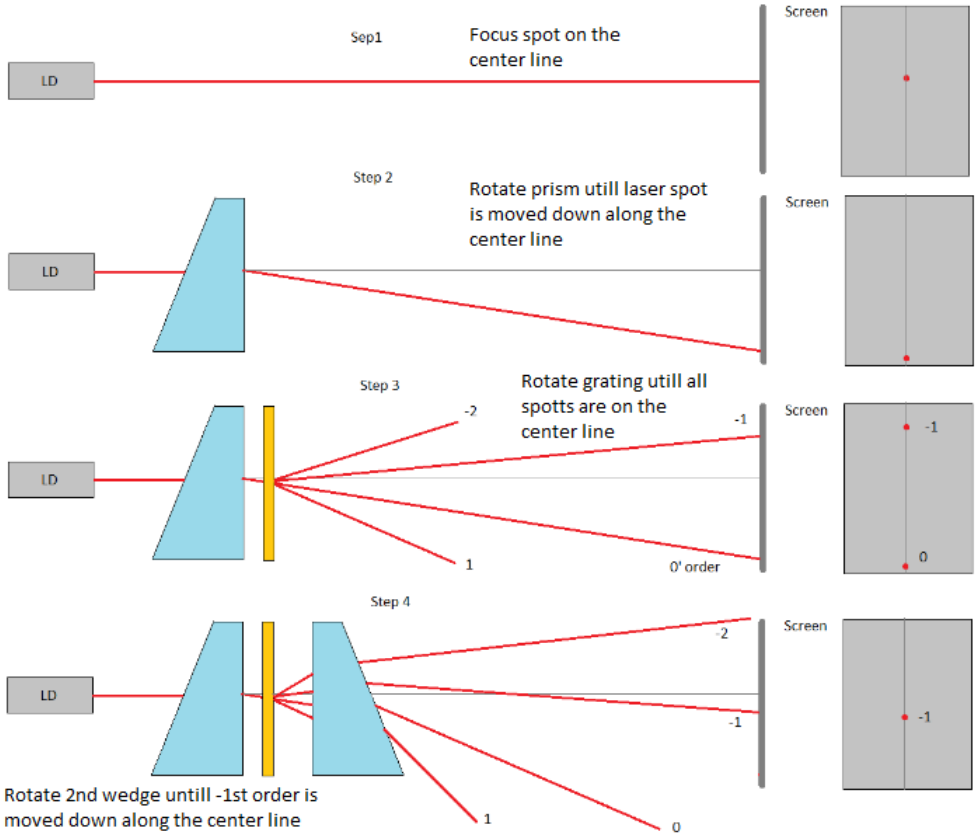

Figure 3.9: Alignment procedure for the wedge prisms and grating.

Next the PGP was tested together with the CCD to evaluate the functionality of the spectral dispersion. The test was done by aiming the setup towards a halogen lamp that had the protective glass removed. A scanning monochromator

was put in front of the halogen lamp to scan for specific wavelength and the result of the PGP configuration was compared to that of an OceanOptics usb spectrometer.

After the PGP had been tested the whole setup was assembled together with the laser in such a way that a Scheimpflug configuration could be found through small adjustments of the components. Figure 3.10 shows the fully assembled but unshielded spectrometer and diode-laser. Figure 3.11 displays a schematic of the setup.

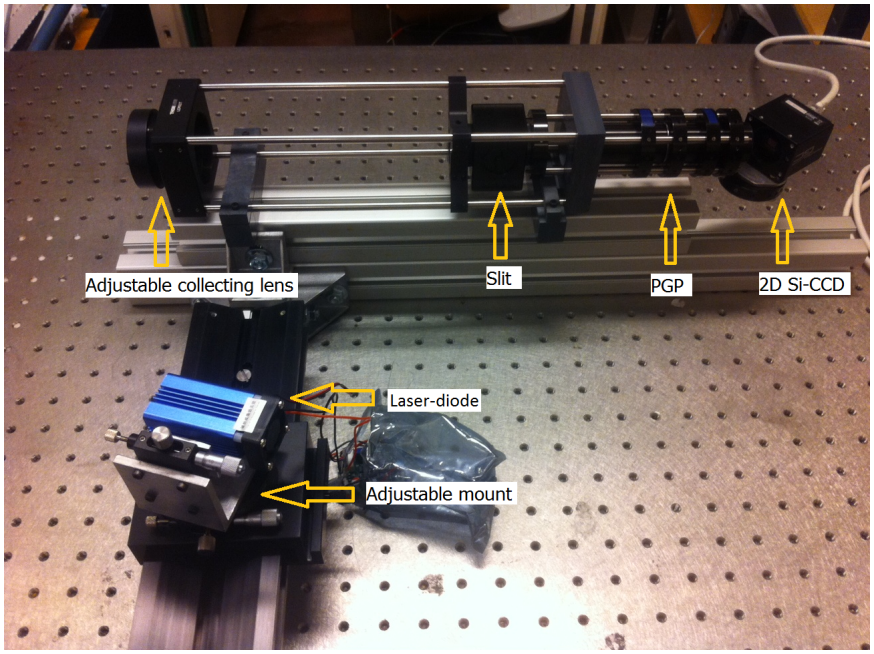

Figure 3.10: Photo of the physical setup. For any practical purposes the setup need to be light-shielded to remove background light and stray backscattered light.

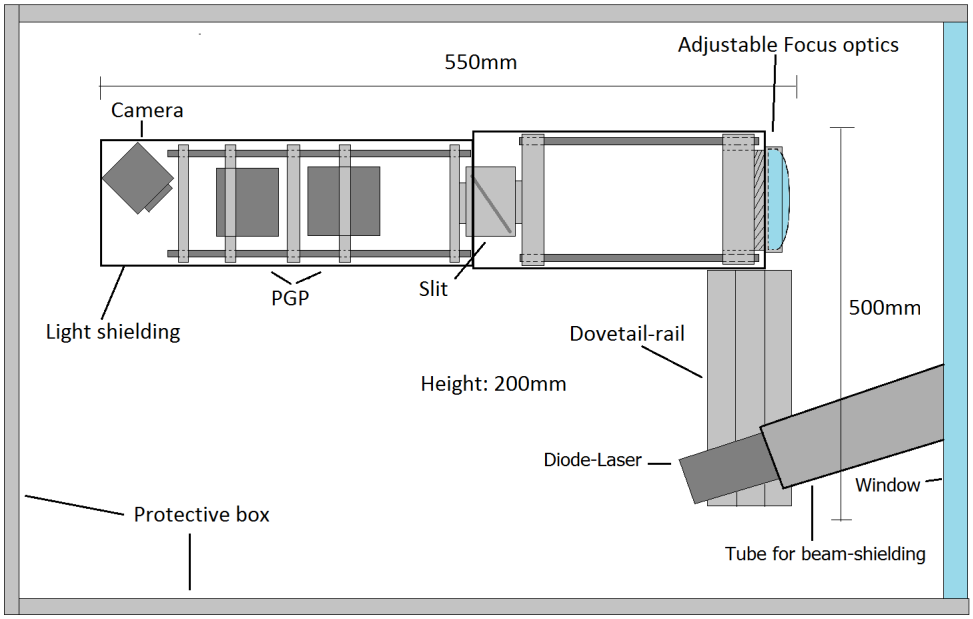

Figure 3.11: Concept drawing of the camera and laser setup. The spectrometer need to be shielded from stray light and the hole setup enclosed to protect the detector but also for laser safety.

Most of the mechanical parts where bought from Edmund optics or Thorlabs but the two manufacturers do not make compatible components so some components had to be handmade to finish the assembly.

All the optics are fixed in position with the exception of the objective that is adjustable in order to achieve focus. The diode laser is mounted on two rotating segments and in turn on a sliding dovetail holder so both the azimuth and elevation angle of the laser may be changed. This is needed to achieve the Scheimpflug-hinge conditions. Figure 3.13 - 3.14 show the distance needed between the focus lens and the diode-laser along with the angle needed to achieve a specific field of view seen in Figure 3.12.

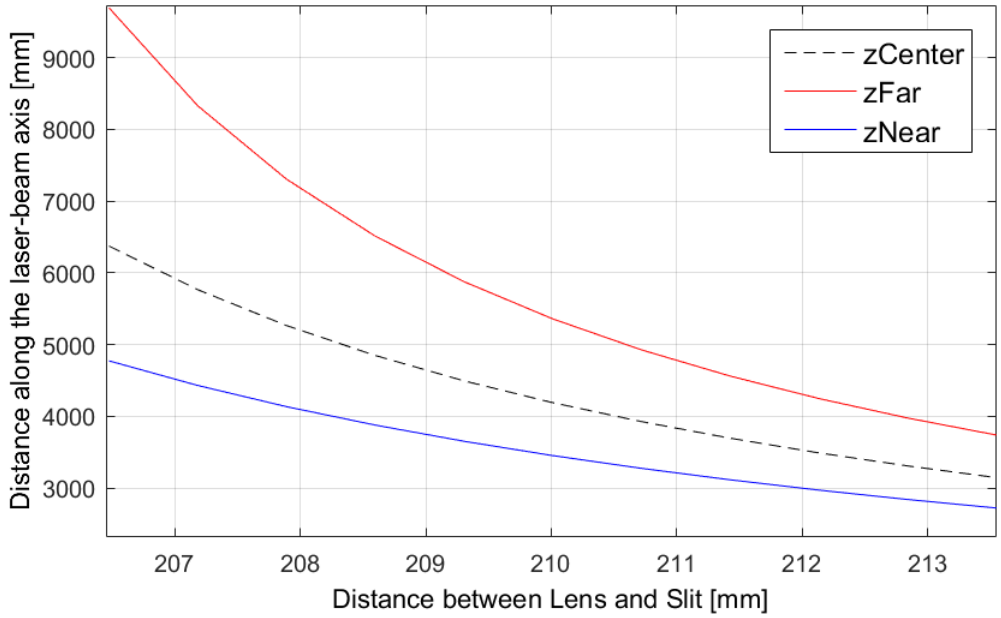

Figure 3.12: Field-of-view for the spectrometer dependent on the distance from the objective-lens to the slit, assuming that f = 200mm and the slit angle $\alpha = 45^o$

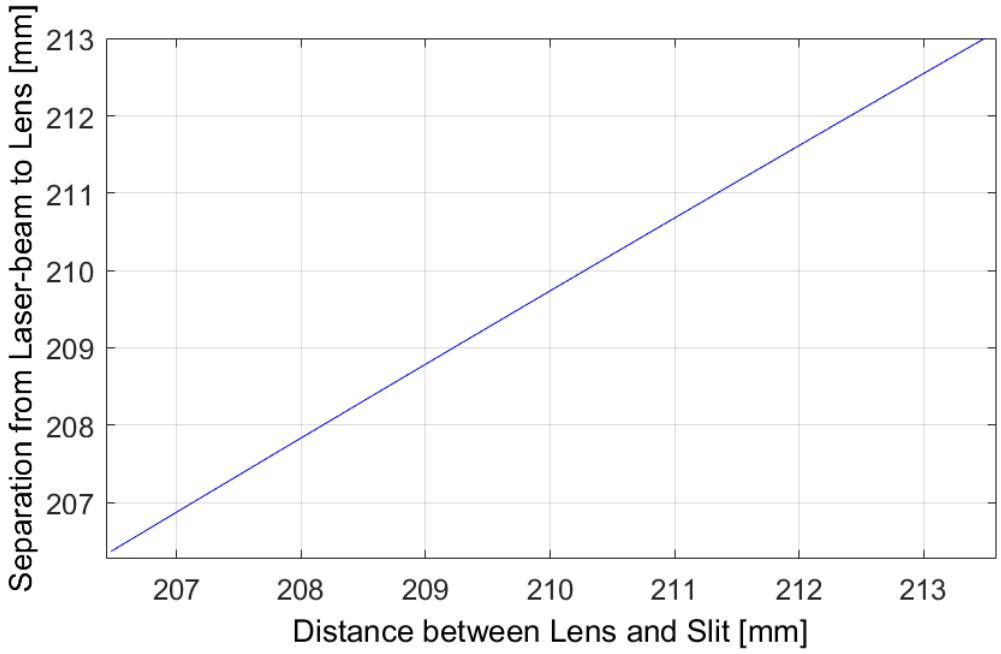

Figure 3.13: Separation distance from the camera to the laser as a function of the distance lci. Assuming that f=200mm and $\alpha = 45^o$

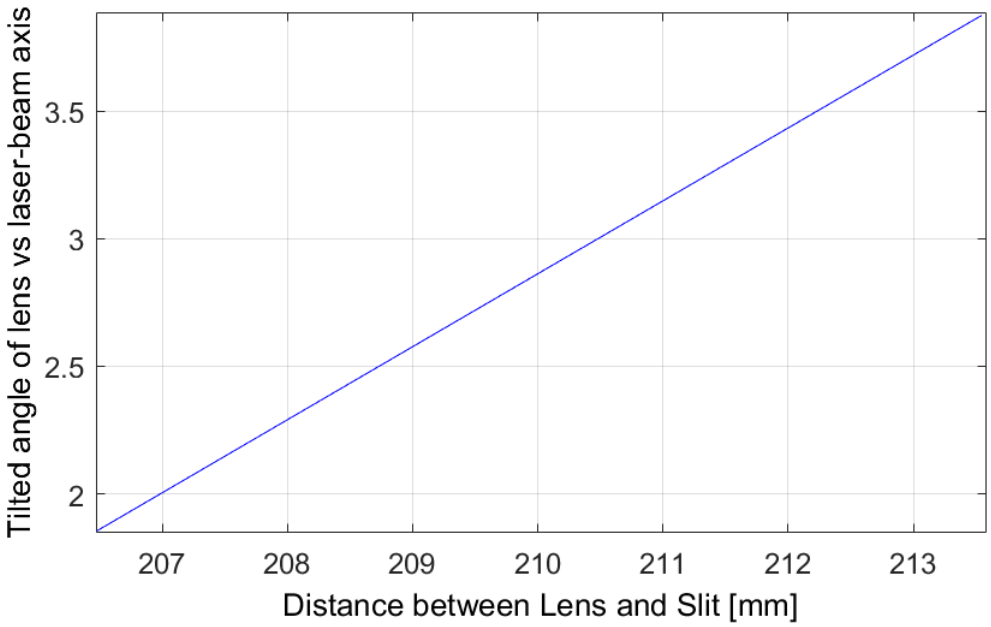

Figure 3.14: Tilt angle of the camera with regard to the laser axis as a function of the distance lci. Assuming that f=200mm and $\alpha = 45^o$

In practice however these values only serve as an initial point. To achieve focus The laser was turned on and pointed to a distant beam-block and then the optics on the laser was focused to achieve a minimum spot on the beam-block. The objective on the spectrometer was then focused to minimize the spot in the detector. And finally the laser was adjusted in height and angle to find the correct spot on the detector.

When the PGP and Scheimpflug-hinge components had been tested together the whole setup was moved to another location and reassembled together with a 5-meter-long test tank filled with water that was used as the test-range. The laser and spectrometer was aimed along the test tank and re-calibrated to compensate for the additional refraction in the water and glass surface of the tank. The recalibration was done by adjusting the focus of the spectrometer and angling of the laser until a focus was achieved on the detector. Tests were performed in the tank with both fluorescent plastic cards, green leaves, phytoplankton and live zooplankton of the genus Daphnia. Figure 3.15 and Figure 3.16 show the experimental setup.

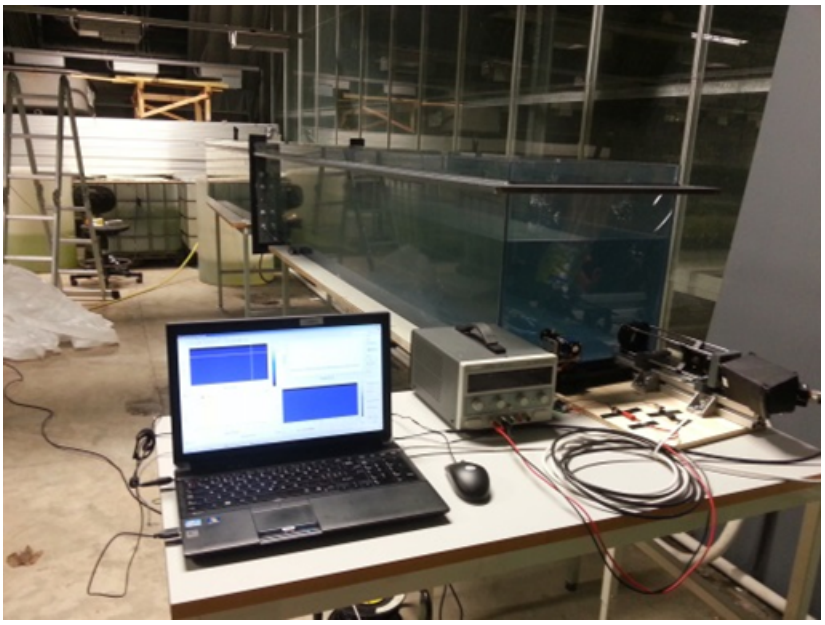

Figure 3.15: Picture of the experimental setup. The laser is positioned at one end of a 5-meter-long tank that is accessible from the top.

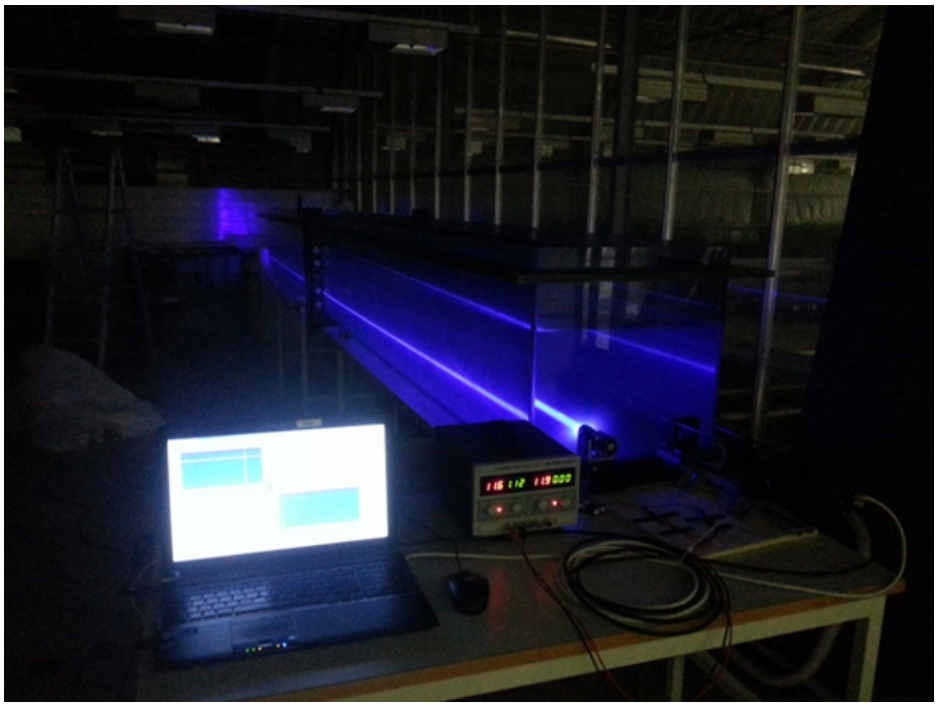

Figure 3.16: Picture of the experimental setup with the laser turned on.

4. Data analysis and results

The data results are presented in the order it was tested. First, the data collected during the assembly and calibration procedures are shown. Secondly, the data from the aquatic tests are displayed and finally some results which includes live zooplankton.

4.1 Calibrations

Figure 4.1 shows 3 images from the initial tests of the spectral dispersion capabilities for the PGP part of the spectrometer. A halogen lamp together with the tunable monochromator was used to test the spectral range of the spectrometer. It was concluded that the spectral bandwidth for the spectrometer would be able to encompass the elastic signal at 445 nm and beyond the chlorophyll fluorescence at 680 nm.

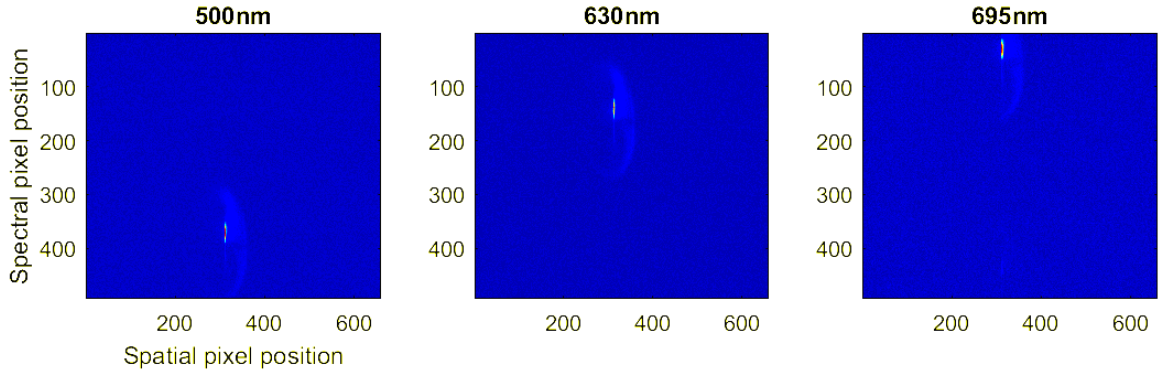

Figure 4.1: 3images taken during the spectrometer PGP test. A halogen lamp was used as a white light source together with a tunable monochromator to create light at different wavelengths. The color indicates pixel intensity where blue is low and red is high-value

After the scanning with the monochromator, the results displayed in figure 4.2 was plotted along one constant Spatial pixel position (pixel nr 362). The result can be seen in figure 4.1. The resulting peaks was compared to the signal captured by the OceanOptics usb spectrometer that was used to monitor the same light emitted from the monochromator. The peaks from the OceanOptics usb spectrometer can be seen in figure 4.3. The wavelength/pixel dependence for the spectrometer was calibrated using the information from figure 4.3. As can be seen in the figures (4.2,4.3) the resulting peaks in the spectrometer are slightly wider which is expected due to the limitations of the slit. The signal for the spectrometer also exhibit more noise. However, at this point the spectrometer was still mostly unshielded since calibrations was being conducted.

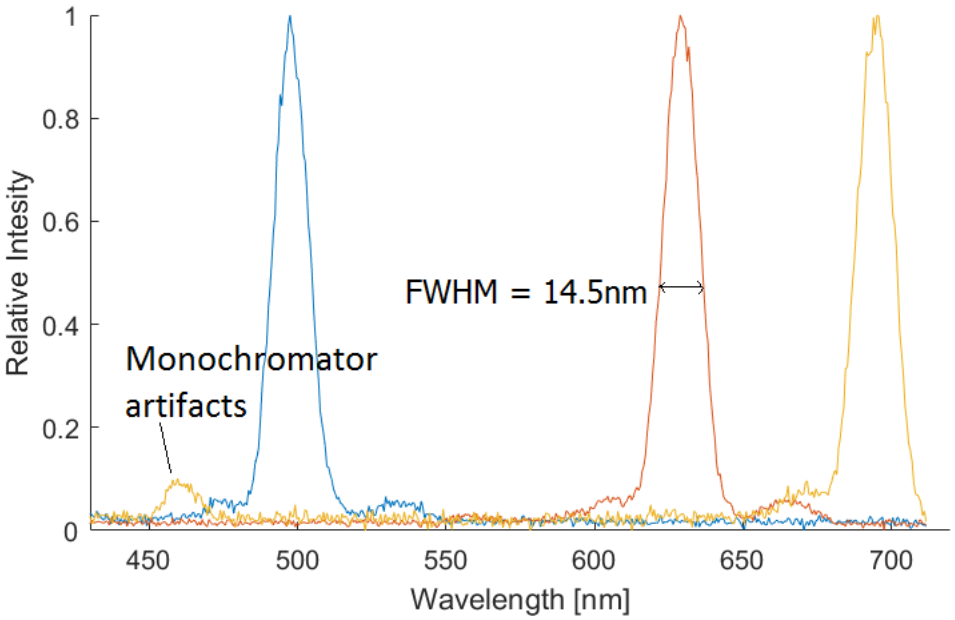

Figure 4.2: Spectral information along one spatial pixel (nr 326) on the ccd. The tunable monochromator had been set to different wavelengths (500, 630 and 695 nm) and images were collected with the CCD.

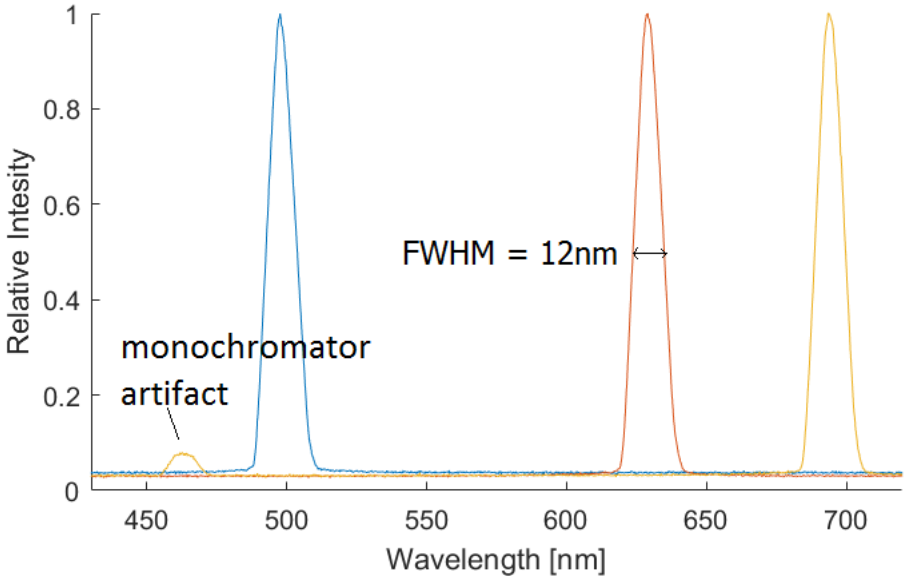

Figure 4.3: Spectral information using an OceanOptics spectrometer. The peaks originate from the same source as figure 4.2. The information is used to determine wavelength/pixel position for the CCD.

To test the spectral response of the full range of the spectrometer, a 90W household halogen lamp was used as a white-light source. The protective glass was removed to allow emission of shorter wavelengths which are normally blocked by the bulb. The melting point for tungsten is 3695K however a halogen is not a perfect blackbody radiator so the halogen lamp was assumed to have a emission spec-

trum close to a 3200K blackbody radiator, a common temperature spectrum for a tungsten-halogen lamp [33]. The blackbody radiation was simulated by Planck's law [21] and plotted against the response of the spectrometer in figure 4.4. The small dip in the spectrometer curve at 620 nm is believed to be from dust on the detector.

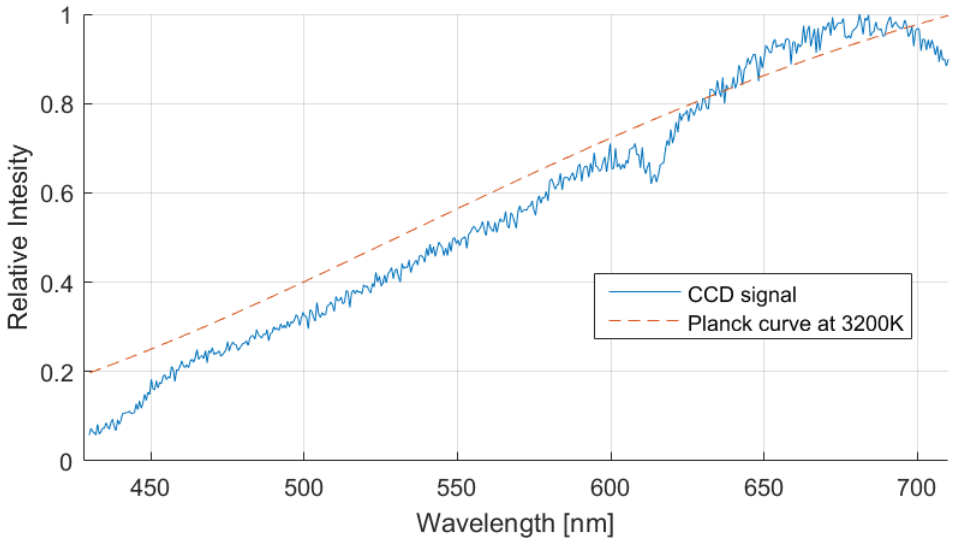

Figure 4.4: Spectral plot at one spatial pixel-position for the CCD. The white light-source consists of a common halogen lamp with the protective glass-bulb removed. The small dip in intensity at ca 620 nm is believed to be from dust on the detector.

4.2 Raman and Fluorescence

Figures 4.5 to 4.13 show results from the tests done with the 5-meter-long test tank filled with tap water. The first tests were done with only water in the tank to determine if the Raman signal from the water could be detected along with the elastic backscatter signal. Figure 4.5 shows a single screen capture of the hole detector with only water in the tank. In figure 4.6 one range pixel position has been selected and the intensity counts plotted as a function of wavelength. Both the Raman-signal and the elastic signal can be seen in the plot. According to the theory at page 9, the Raman-peak should be at 520nm. Besides calibration error this could be caused by the laser did not emit exactly 445 nm which would also shift the position of the assumed Raman peak.

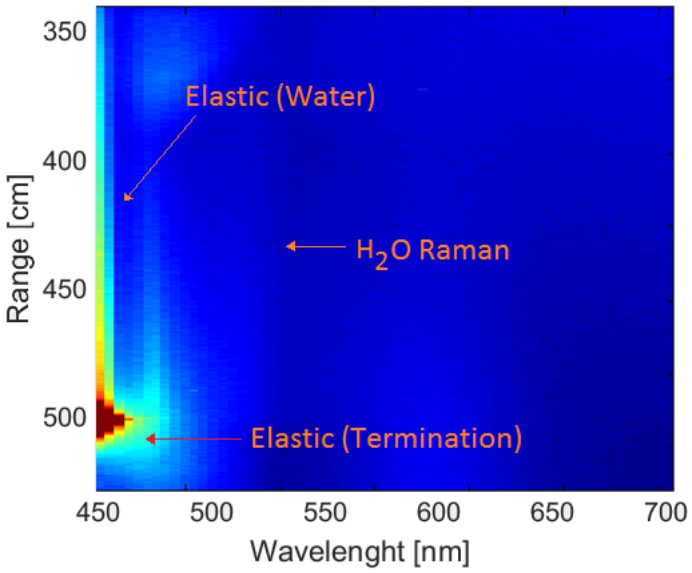

Figure 4.5: Full image caption from the CCD. In the current setting the CCD is binned to 61 spectral pixels. The strong signal in the bottom left corner is from the termination.

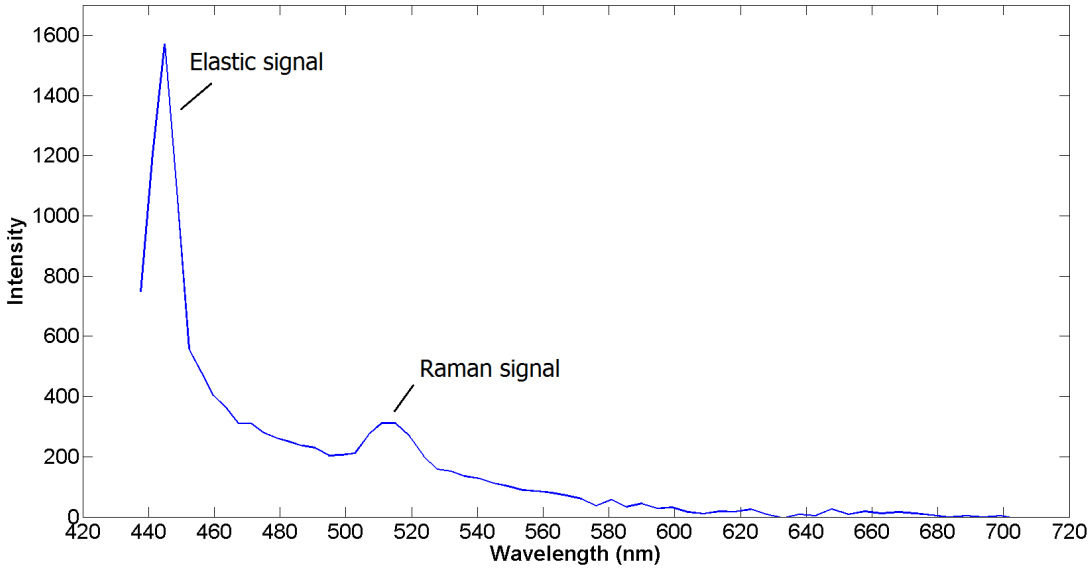

Figure 4.6: Intensity information at one spatial pixel-range (pixel nr 300). Both the elastic signal and the water-Raman signal can be seen. The wavelength calibration is somewhat off in this image. The Raman peak should be at 520nm

Figure 4.7 shows how the spectral channels of interest can be singled out and plotted against the distance. This can be usefully when studying a certain spectrum. It is also possible to compare intestines for different wavelengths at different range. In the figure the elastic band and the Raman band have been selected. The termination peak has not been diffused enough resulting in saturation at end range.

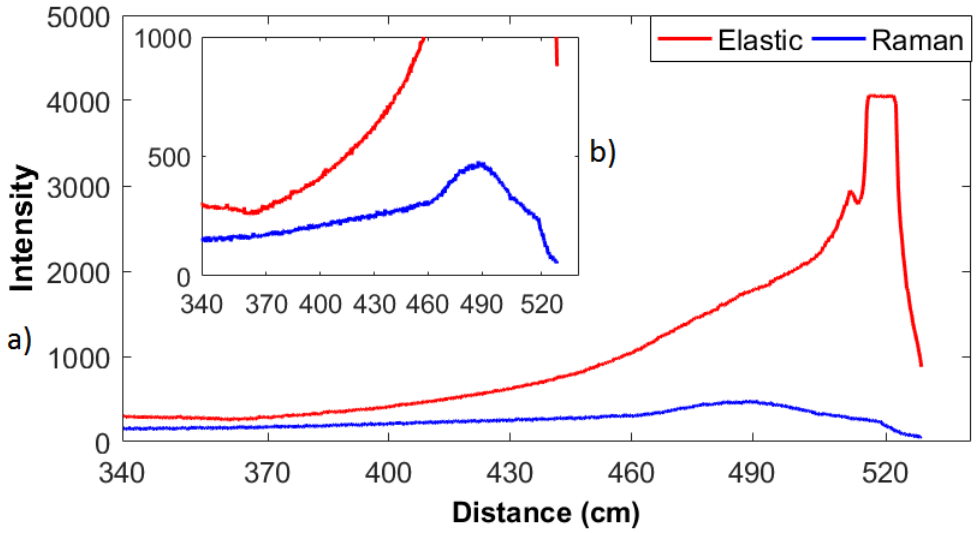

Figure 4.7: Simultaneous plot of the elastic and Raman signal. both figure a) and b) are the same plot with different scaling. In this case the elastic signal saturates the detector at the termination range. The Raman signal drops in strength just before the termination.

The ability to detect fluorescence was initially tested using fluorescing plastic cards seen in figure 4.8. The cards where moved along the the laser-beam in the test tank. Figure 4.9 is a composition of 3D plots from several still frames. The fluorescence from the cards can be seen moving along the range while the elastic termination signal in the top left corner remains stationary.

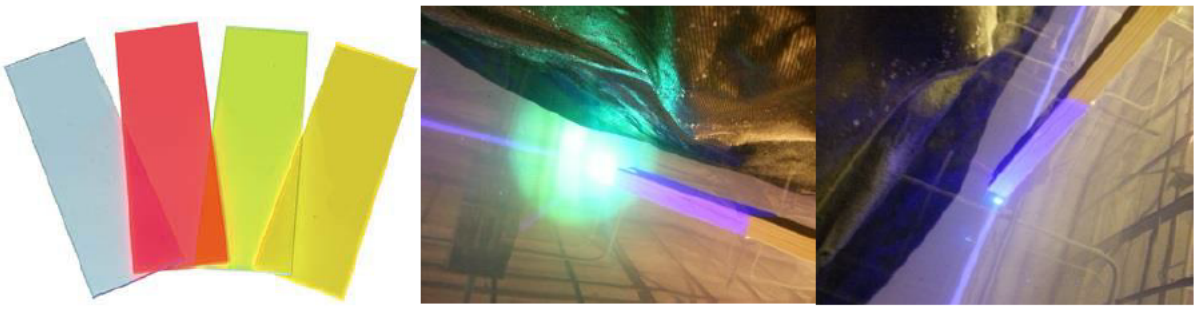

Figure 4.8: The left image shows fluorescing plastic cards that where put into the beam and moved along the tank. The two images to the right show leaves attached to a stick and moved along the beam.

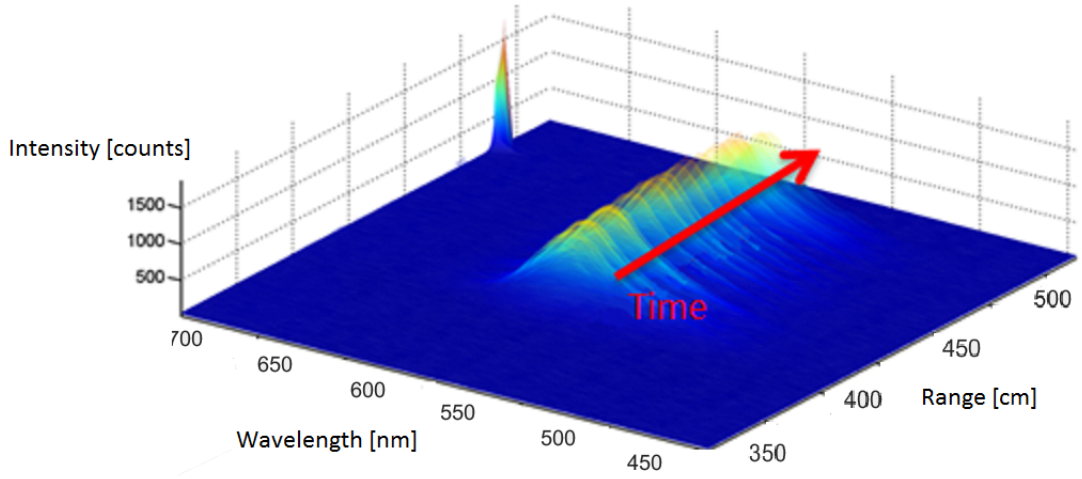

Figure 4.9: 3D plot of the fluorescence signal from a moving fluorescing card. In the top left corner the peak from termination is also visible.

Figure 4.10 displays the fluorescence signal as the fluorescing cards are passed through the laser-beam plotted with wavelength, range and time. The surfaces shown are iso-surfaces above a set signal threshold value. In the figure we can see the same elastic termination

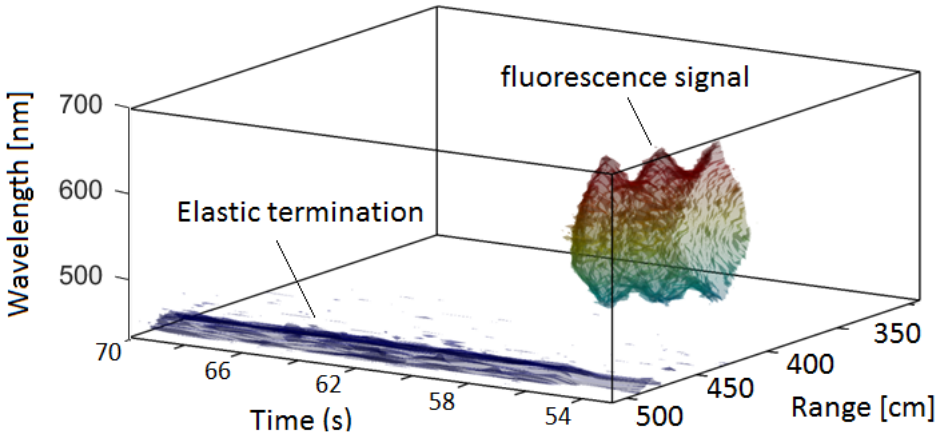

Figure 4.10: 3D plot of the fluorescence signal from a plastic card and the elastic termination. The termination signal is attenuated as the cards pass through the beam. In this case there is no intensity information in the color.

Figure 4.11 displays the signal from the leaves shown in figure 4.8 moving along the test tank. The figure shows both the elastic signal from the leaves and the fluorescence from chlorophyll described in the theory. The elastic termination signal can also be seen in at the start of the timescale. This is due to that only a portion of the beam is being blocked. If the scattering object is sufficiently small or translucent then it would be possible to detect several objects at different range at the same time.

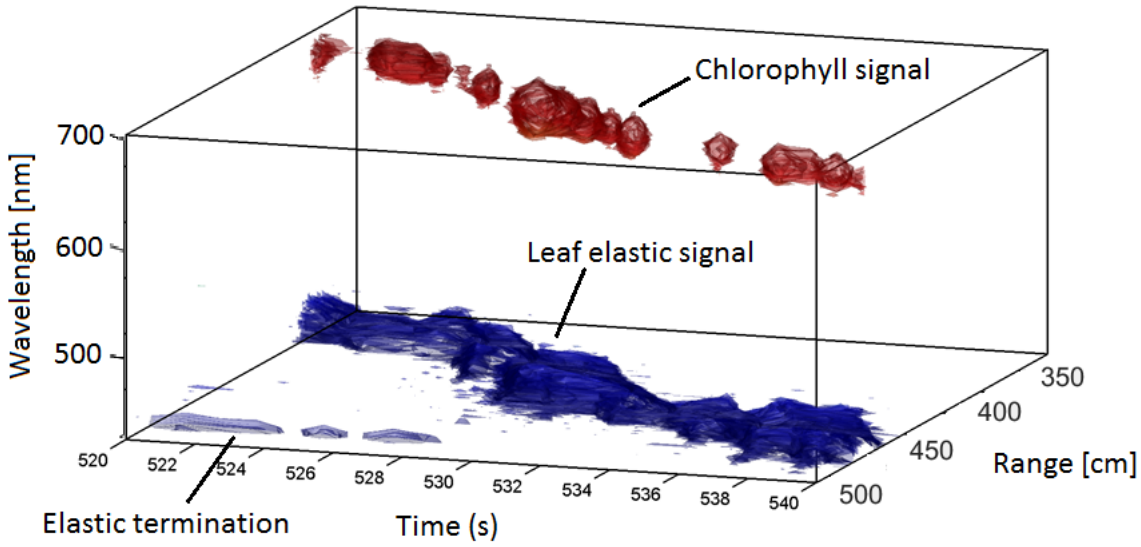

Figure 4.11: 3D plot of the signal from a leaf moving along the beam. The red surface is chlorophyll fluorescence from the leaf and the dark blue is elastic signal from the same leaf. The termination signal is blocked when the leaf intersects the beam

Figure 4.12 show the result of phytoplankton being inserted into the laser-beam. As with the leaf in figure 4.11 the phytoplankton exhibits both elastic backscattering and fluorescence from chlorophyll.

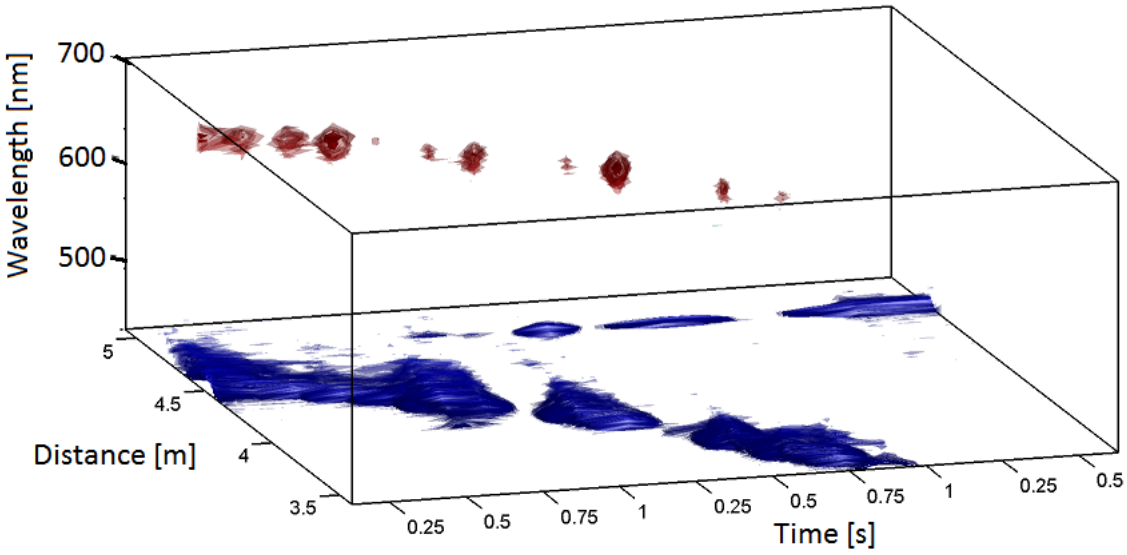

Figure 4.12:

4.3 Plankton signal

Figure 4.13 shows a detected zooplankton (Daphnia) event. The image displays only the elastic signal at different times and range. The termination can be seen at max range along the duration of the capture. At 190 s there is an event where a zooplankton enters the laser beam a range of 430 cm.

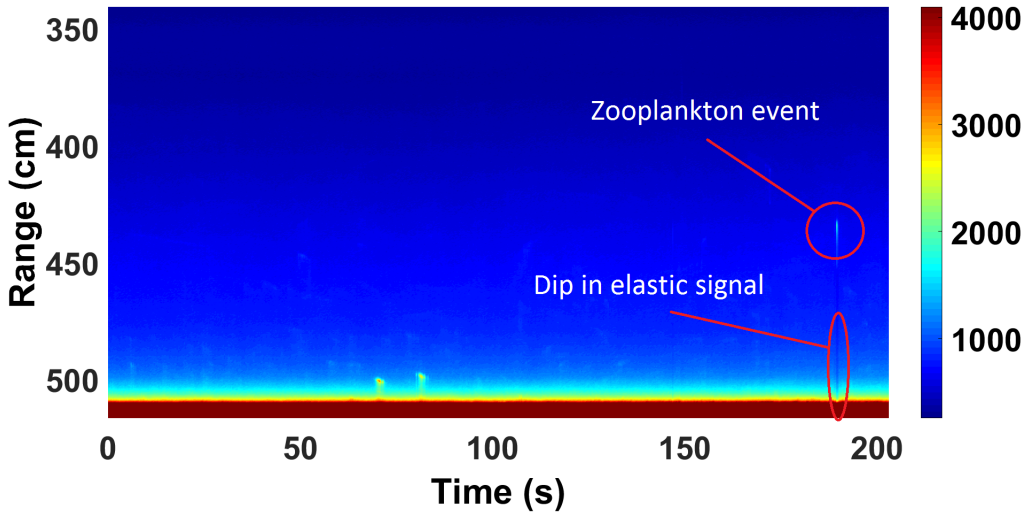

Figure 4.13: The elastic channel over time. The figure shows a zooplankton elastic event.

Figure 4.14 shows a similar plot as figure 4.13 with another zooplankton event. Data from the event is extracted and plotted at constant time or distance in figure 4.15. In figure 4.15 a), the zooplankton event can clearly be seen at around time frame nr 2586. Whoever the resolution is not good enough to resolve any oscillations of the legs. There is one repeating peak at a 15 frame interval, it is however only 3 peaks and not enough to draw any conclusions. There is also a challenge in inserting the zooplankton into the laser-beam and having them staying long enough in the beam (and correctly orientated) to collect satisfactory data. In b) we can se the elastic signal from both the zooplankton and the termination at a fixed time-frame. The event itself is clearly distinguishable from the termination. The distance for the event is not entirely clear in this case due to the slope on the right of the event-peak. Both of these issues might be resolved with fine-tuning the setup and more experience using it.

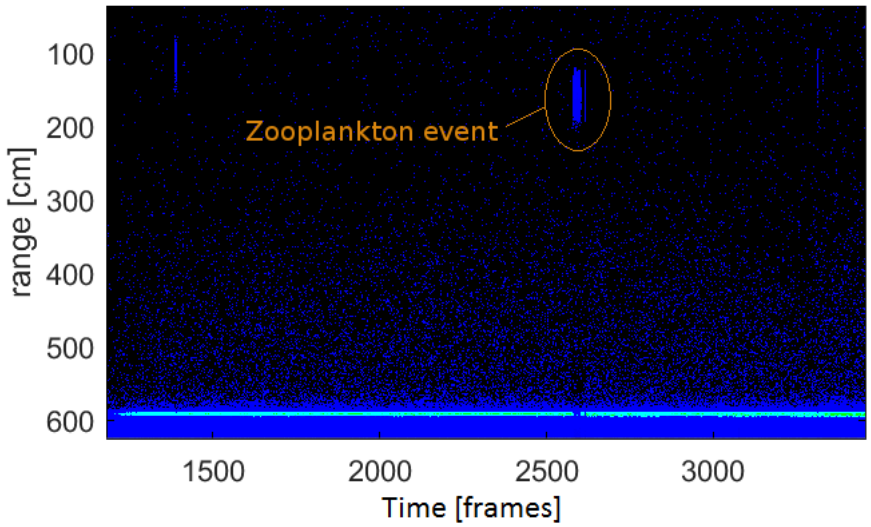

Figure 4.14: Zooplankton event using elastic channel. figure 4.15 are corresponding time and distance plots for the event.

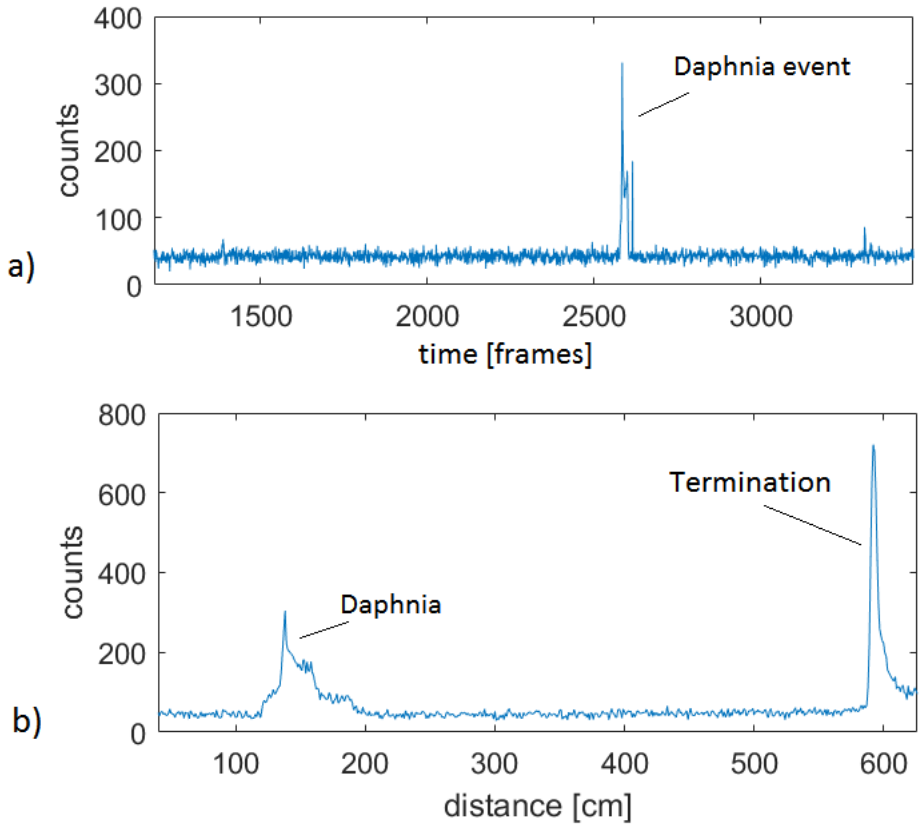

Figure 4.15: Both plots contain data extracted from the same dataset as figure 4.14. a) Time dependent elastic signal at constant distance = 141cm. b) Distance dependent elastic signal at time = 2584 frames.

5. Discussion and conclusion

The system we have constructed is a compact inelastic hyperspectral LiDAR capable of detecting small sparse particles (plankton) and providing both spectral and range information about them and the surrounding medium. The current system is capable of having 61 spectral bands over the range of 440 nm - 700 nm and it is capable of capture both the elastic signal from the water and the inelastic signals such as fluorescence from chlorophyll and Raman scattering from water. Since the Raman cross-section for water is known it would possible to estimate beam-FOV overlap function and thus calibrate other scatter magnitudes to the Raman-signal [34]. The system has the ability to reduce the number of spectral bands in order to achieve higher frame rates. So far, we have not been able to detect the oscillation in the elastic cross-section signal for zooplankton. Compared to flying insects, whose oscillating cross section caused by their wing beats has been detected previously, the legs etc on zooplankton are much smaller and thus give rise to a substantially smaller oscillation of their cross section. Better calibration and system optimization could possibly let us detect these small oscillations.

So far the system has only been tested in a 5-meter-long test tank but the range could be extend much further. This is however limited to the transmission of the water. The system is limited for close distances (a practical limit of around 1m can bee expected with the current setup. This will however also limit the max distance as we see in figure 3.12). The range can be improved by a larger sensor or by adapting a collecting lens with shorter focal length. However, the ability for 0-distance cannot be achieved unless the lidar is moved up from the surface of the water. An alternative approach would be to submerge the LiDAR and point it toward the surface if near surface signal is of interest.

An issue that could pose a problem is how the zooplankton reacts to the laser-light. Most marine animals have photoreceptors capable of detecting blue light and many zooplankton exhibit both positive or negative phototaxis [35–37] depending on time of day. It can be argued that the effect of the phototaxis is negligible due to the slow swim-speed of the plankton. There is also the ethical issue with the risk of blinding the plankton. Most plankton have eyes designed to detect light rather than focus it, and with the attenuation of the light through the water the damage should be minimal. Even if there would be permanent damage one could argue that in many plankton study approaches (nets etc.) the plankton would perish anyway.

An issue of more concern would be eye damage to larger marine animals. In this case one would need to do a case-by-case study of local marine life to determine safety precautions. There has been some study done on laser safety for marine animals [38]

6. Outlook

Compared to other LiDAR systems based on pulsed lasers the system described here has several advantages. Due to the recent improvements in diode lasers, such as GaN laser diodes, the cost for our system would be a fraction of a pulsed laser system. The weight of the laser diode, optics (including fixtures) and detector is less than 500 g, with the total weight determined by the mechanics and enclosure making it much lighter than a pulsed laser system. The power consumption of the GaN diode and detector is also very low, needing only a low voltage source to power it.

The very low cost and weight of the system could make it widely accessible with many possible application beyond that of zooplankton monitoring. The size and weight of the system could make it possible to use drones to reach inaccessible areas or for autonomous monitoring. In the case of atmospheric use, laser safety is a serious concern and has to be considered carefully.

7. Bibliography

[1] Iain Suthers and David Rissik. *Plankton: A Guide to Their Ecology and Monitoring for Water Quality*. Csiro Publishing, 2009.

[2] Dieter Ebert. *Ecology, Epidemiology, and Evolution of Parasitism in Daphnia*. 2005. ISBN-10: 1-932811-06-0.

[3] Hobday A.J, Okey T.A, Poloczanska E.S, Kunz T.J, and Richardson A.J. Impacts of climate change on australian marine life: Part c. literature review. Technical report, Report to the Australian Greenhouse Office, Canberra, Australia, September 2006.

[4] W. Lampert. The adaptive significance of diel vertical migration of zooplankton. *Functional Ecology*, 3(1):21–27, 1989.

[5] Zooplankton acoustic profiler. http://www.oceannetworks.ca/zap-data-saanich-inlet, Aug 16 2013. urldate: 2015:05:15.

[6] Mark C. Benfield, Philippe Grosjean, Phil F. Culverhouse, Xabier Irigoien, Michael E. Sieracki, Angel Lopez-Urrutia, Hans G. Dam, Qiao Hu, Cabell S. Davis, Allen Hansen, Cynthia H. Pilskaln, Edward M. Riseman, Howard Schultz, Paul E. Utgoff, and Gabriel Gorsky. Research on automated plankton identification. *Oceanography*, 20(2):172–187, June 2007.

[7] S.K. Jericho, J. Garcia-Sucerquia, Wenbo Xu, M.H. Jericho, and H.J. Kreuzer. Submersible digital in-line holographic microscope. *Review of scientific instruments*, 77, 2007. doi: 10.1063/1.2193827.

[8] H. Sun, P.W. Benzie, N. Burns, D.C. Hendry, M.A. Player, and J. Watson. Underwater digital holography for studies of marine plankton. *Phil. Trans. R. Soc. A*, 366:1789–1806, Januari 2008. doi: 10.1098/rsta.2007.2187.

[9] Jüri Lapimaa Alexei Lisin Larisa Poryvkina Sergey Babichenko, Alexander Dudelzak and Alexandre Vorobiev. Locating water pollution and shore discharges in costal zone and inland waters with fls lidar. *EARSeL eProceedings 5*, pages 32–41, Januari 2006.

[10] James H. Churnside, James J. Wilson, and Viatcheslav V. Tatarskii. Airborne lidar for fisheries applications. *Optical Engineering*, 40(3):406–414, March 2001. doi: 10.1117/1.1348000.

[11] Joseph A. Shaw, James H. Churnside, James J. Wilson, Nicole E. Lerner, Rianon R. Tiensvold, Patricia E. Bigelow, and Todd M. Koel. Airborne lidar mapping of invasive lake trout in yellowstone lake. Technical report, Electrical and Computer Engineering Department, 610 Cobleigh, Montana State University, 2008.

[12] James H. Churnside, David A. Demer, and Behzad Mahmoudi. A comparison of lidar and echosounder measurements of fish schools in the gulf of mexico. *ICES Journal of Marine Science*, 60:147–154, 2003. doi: 10.1006/jmsc.2002.1327.

[13] James H. Churnside and Richard E. Thorne. Comparison of airborne lidar measurements with 420 khz echo-sounder measurements of zooplankton. *Optical Society of America*, 60:147–154, 2005. doi:10.1006/jmsc.2002.1327.

[14] Richard L. Collins Tim Veenstra James J. Wilson Evelyn D. Brown, James H. Churnside and Kevin Abnett. Remote sensing of capelin and other biological features in the north pacific using lidar and video technology. *ICES Journal of Marine Science,*, 59:1120–1130, 2002. doi:10.1006/jmsc.2002.1282.

[15] James H. Churnside. Lidar detection of plankton in the ocean. Technical report, NOAA Earth System Research Laboratory, 2007.

[16] Mikkel Brydegaard, Aboma Merdasa, Alem Gebru, Hiran Jayaweera, and Sune Svanberg. Realistic instrumentation platform for active and passive optical remote sensing. *Applied Spectroscopy*, 0(0):1–14, 2016. doi: 10.1177/0003702815620564.

[17] Mikkel Brydegaard, Alem Gebru, and Sune Svanberg. Super resolution laser radar with blinking atmospheric particles - application to interacting flying insects. *Progress In Electromagnetics Research*, 147:141–151, 2014.

[18] Mikkel Brydegaard. Towards quantitative optical cross sections in entomological laser radar - potential of temporal and spherical parameterizations for identifying atmospheric fauna. *PLoS ONE*, 10(8), 2015. doi: 10.1371/journal.pone.0135231.

[19] Liang Mei and Mikkel Brydegaard. Continuous-wave differential absorption lidar. *Laser Photonics Rev*, 6:629–636, 2015. doi: 10.1002/lpor.201400419.

[20] H. M. Merklinger. *Focusing the View Camera*. 2010. Dartmouth, Nova Scotia, isbn: 0-9695025-2-4.

[21] S.Svanberg. *Atomic and Molecular Spectroscopy, Basic Aspects and Practical Applications*. 4 edition, 2003.

[22] Grimm Bernhard. *Chlorophylls and Bacteriochlorophylls Biochemistry, Biophysics, Functions and Applications*. Advances in Photosynthesis and Respiration, 1572-0233 ; 25. Springer, 2006. isbn-13 978-1-4020-4516-5.

[23] B. Greg Mitchell and Dale A. Kiefer. Chlorophyll a specific absorption and fluorescence excitation spectra for fight-limited phytoplankton. *Deep-Sea Research*, 35(5):639–663, 1988.

[24] Maria Vernet and Carl J. Lorenzen. The presence of chlorophyll b and the estimation of phaeopigments in marine phytoplankton. *Journal of Plankton Research*, 9(2):255–265, 1987. doi: 10.1093/plankt/9.2.255.

[25] http://www.photosynthesis.ch/fluorescence.htm.

[26] Gregory W. Faris and Richard A. Copeland. Wavelength dependence of the raman cross section for liquid water. *Applied Optics*, 36(12):2686–2688, 1997. doi: 10.1364/AO.36.002686.

[27] Maurizio Becucci, Stefano Cavalieri, Roberto Eramo, Lorenzo Fini, and Marzia Materazzi. Accuracy of remote sensing of water temperature by raman spectroscopy. *Applied Optics*, 38(6):928–931, 1999. doi: 10.1364/AO.38.000928.

[28] C. P. Artlett and H. M. Pask. Optical remote sensing of water temperature using raman spectroscopy. *Optics Express*, 23(25):31844–31856, 2015. doi: 10.1364/OE.23.031844.

[29] Mauri Aikio. Hyperspectral prism-grating-prism imaging spectrograph, June 2001. Phd thesis. Deparment of Electrical Engineering of the University of Oulu.

[30] http://www.gratinglab.com/Information/Technical_Notes/TechNote4.aspx.

[31] http://www.edmundoptics.com/optics/gratings/transmission-gratings/2934/.

[32] Luca A. van Duren and John J. Videler. Escape from viscosity: the kinematics and hydrodynamics of copepod foraging and escape swimming. *The Journal of Experimental Biology*, 206:269–279, 2003.

[33] Michael W. Davidson. Tungsten-halogen incandescent lamps. http://zeiss-campus.magnet.fsu.edu/articles/lightsources/tungstenhalogen.html.

[34] A. J. Lawaetz and C. A. Stedmon. Fluorescence intensity calibration using the raman scatter peak of water. *Applied Spectroscopy*, 63(8):936–940, August 2009. doi: 10.1366/000370209788964548.

[35] D. E. Stearns and R. B. Forward. Photosensitivity of the calanoid copepod a cartia tonsa. *Marine Biology*, (82):85–89, 1984.

[36] Peter J. Barile, Allan W. Stonerb, and Craig M. Young. Phototaxis and vertical migration of the queen conch (strombus gigas linne) veliger larvae. *Journal of Experimental Marine Biology and Ecology*, (183):147–162, 1994.

[37] Gaspar Jekely, Julien Colombelli, Harald Hausen, Keren Guy, Ernst Stelzer, Francois Nedelec, and Detlev Arendt. Mechanism of phototaxis in marine zooplankton. *Nature*, 456:395–400.

[38] Heather M. Zorn, James H. Churnside, and Charles W. Oliver. Laser safety thresholds for cetaceans and pinnipeds. *Marine mammal science*, 16(1):186–200, Januari 2000.